This is to certify that the
thesis entitled

DESIGN AND ANALYSIS OF MESO-SCALE COOLING AND
STATIC MIXING DEVICES

presented by

RAMKUMAR SUBRAMANIAN

has been accepted towards fulfillment
of the requirements for the

Master of   degree in   Mechanical Engineering
Science

_____
Major Professor's Signature

_____5/14/04_____
Date

PLACE IN RETURN BOX to remove this checkout from your record.
TO AVOID FINES return on or before date due.
MAY BE RECALLED with earlier due date if requested.

DATE DUE	DATE DUE	DATE DUE

6/01 c:/CIRC/DateDue.p65-p.15

DESIGN AND ANALYSIS OF MESO-SCALE COOLING AND STATIC MIXING DEVICES

BY

RAMKUMAR SUBRAMANIAN

A THESIS

Submitted to
Michigan State University
in partial fulfillment of the requirements
for the degree of

MASTER OF SCIENCE

Department of Mechanical Engineering

2004

ABSTRACT

DESIGN AND ANALYSIS OF MESO-SCALE COOLING AND STATIC MIXING DEVICES

By

Ramkumar Subramanian

In recent years, there has been a growing emphasis in manufacturing research on the design and fabrication of Microtechnology-based Energy and Chemical Systems (MECS). MECS are mesoscopic devices, which use embedded microstructures to enhance heat & mass transfer and chemical reactions. Mesomachines are expected to provide a number of important functions where a premium is placed on mobility, compactness, or point application. The first part of this thesis investigates the design aspects for fabricating a two-fluid counter flow meso-scale heat exchanger. For this investigation, a finite element analysis was carried out using *Abaqus CAE* to determine the limits on fin aspect ratios in two-fluid microchannel arrays produced by diffusion bonding. The second part of this thesis addresses the issue of using Functionally Gradient Materials (FGM), achieved by spatially varying the compositional ratio between two powders, to fabricate an active cooled and efficient meso-scale heat exchanger. Coupled fluid-thermal-structural finite element analysis was done using *Ansys Multiphysics 7.*0 to minimize residual thermal stresses in the heat exchanger. The final part of this thesis deals with the design of ribbed ducts to facilitate mixing of two liquids in microfluidic devices. *Fluent 6.*0, a computational fluid dynamics package, was used to determine the extent of mixing in the ribbed ducts for various combinations of fluid properties and inlet conditions.

Man is made by his belief. As he believes, so he is.
Bhagavad-Gita

To my loving parents and sister

ACKNOWLEDGMENTS

TABLE OF CONTENTS

LIST OF TABLES

LIST OF FIGURES
(Images in this thesis are presented in color)

1. INTRODUCTION

Over the last ten years, there has been a growing interest in the use of low-cost, engineering materials to fabricate Micro Energy and Chemical Systems (MECS). MECS are multi-scale fluidic devices, which rely on embedded micro-scale features to process bulk fluids for portable and distributed energy and chemical systems applications. MECS are expected to provide a number of important functions where a premium is placed on mobility, compactness, or point application. Examples include miniature refrigerators for high-speed electronics portable power packs based on combustion [1] and miniature chemical reactors for on-site waste processing [2].

One advantage of MECS devices over same-sized conventional devices is that they have greater surface area available for heat transfer, reaction, separations, etc. The overall size of MECS devices places them in the mesoscopic regime, i.e. in a size range between macro objects such as automobile engines and laboratory vacuum pumps, and the intricate MEMS based sensors that reside on a silicon chip. Thus MECS, although having microfeatures, are large by MEMS standards straddling the size range between the macro- and micro- worlds. This large surface area to volume ratio accounts for the high rates of heat and mass transfer within MECS devices.

The internal processes of these devices rely on length scales that are much smaller than traditional systems. For thermal and chemical applications, a small characteristic size provides the benefits of high rates of heat and mass transfer, large surface-to-volume ratios, and the opportunity of operating at elevated pressures. For other more

mechanically operated meso machines such as generators and motors, small dimensions imply rapid response and compact design. Furthermore, these systems can often be volume produced resulting in substantial cost reduction of each device.

In the energy area, MECS will find increasingly important uses where small scale heat engines, heat pumps and refrigerators are needed. For example, the development of miniature refrigerators could provide point cooling of high speed electronics and communication equipment for enhancing performance. Also, power packs based on combustion rather than electrochemistry could extend operating times of electronic devices by a factor of ten. In the area of chemical processing, miniaturized chemical reactors could provide on-site neutralization of toxic chemicals thereby eliminating the need for transport and burial.

Because many MECS devices rely on fluidic processes, the same technology can be applied to biological applications. Miniaturized bioreactors could provide precisely regulated environments for small groups of cells to enhance their production of therapeutic drugs, or the detection of toxic compounds. Such bio-applications could range from benchtop research to large scale production facilities. This thesis is an attempt to design MECS devices which can be used for a variety of purposes.

1.1 LIMIT ON ASPECT RATIO IN TWO-FLUID MICRO-SCALE HEAT EXCHANGER

The first part of the thesis focuses on the theoretical limits on fin aspect ratios within two-fluid micro-channel arrays produced by diffusion bonding. The counter-flow device is

comprised of alternating layers of micro-channels, which allow the two fluids to flow in opposite directions separated, by fins. The objective was to interpret the span of the fin as a function of the fin thickness with the help of a finite element model.

Finite element analysis was performed on a model which assumes the micro-lamination fabrication method. Micro-lamination involves the patterning and bonding of thin layers of material called laminae [3]. Laminae could be metal shims or polymer films having the desired mechanical, thermal and chemical properties important to the device function. The process begins by surface machining, or through cutting of a single laminate in the desired pattern. Once the pattern is cut, the laminates are surface treated to enhance the diffusion bonding and stacked in a prearranged order. The stack is then bonded together forming a single block of material. For the method to have utility, a machining method capable of fabricating structures in the laminating material is needed. The method must be versatile, easy to use, and capable of rapidly machining (with through-cuts and surface texturing) a wide variety of materials. Laser numerically controlled micromachining satisfies these requirements. Other techniques such as through-mask electrochemical machining and stamping are applicable to laminate forming.

Micro-lamination techniques have been used to fabricate MECS devices for advanced climate control [4], solvent separation [5], micro combustion [6], fuel processing [7], fluid compression [8], microdialysis [9] and dechlorination among others. Several research institutions and industrial companies have developed micro-lamination approaches for producing MECS devices [3, 10]. In all, systems of micro-channel arrays

have been constructed in a wide array of materials including copper, stainless steel, titanium, nickel, intermetallics and various polymers with features as small as five μm.
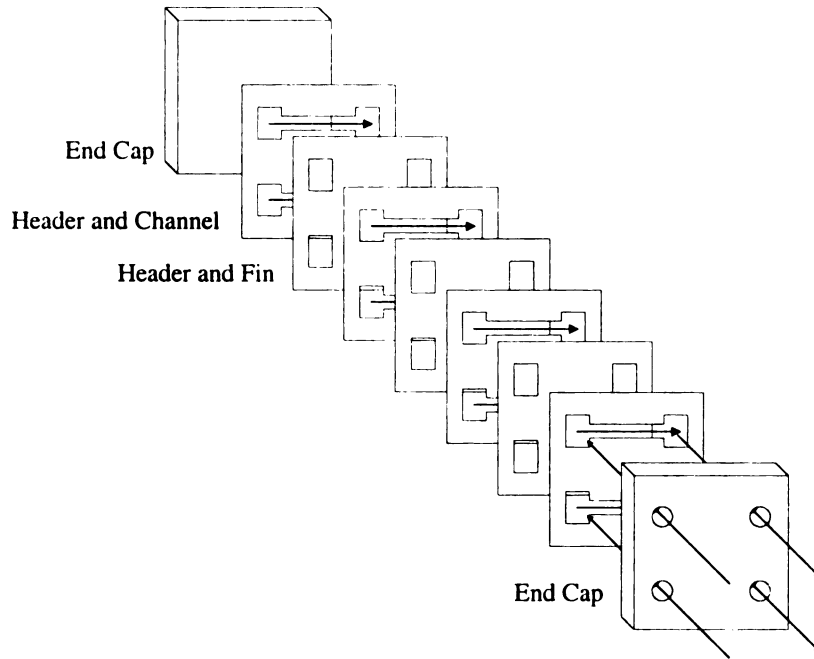
Figure 1: Micro-lamination scheme used to fabricate a dual micro-channel array with arrows indicating direction of flow

In the case of heat transfer, the function of a typical micro-channel heat exchanger is to transmit the heat from one fluid stream into a second fluid stream. Several different approaches can be used to accomplish this task. The most efficient heat transfer methods tend to interleave the two fluids in an alternating succession of cross-flow or counter-flow channels. In particular, counter-flow channels are known to provide better temperature distributions along the length of heat exchangers when compared to co-flow heat exchangers [11]. Whereas, in the case of single fluid flow, micro-channels with relatively high aspect ratio's have been fabricated successfully even in hard-to-produce

materials [12], the aspect ratio is generally constrained in two-fluid micro-scale heat exchangers because of the more complex geometry. This research investigates the theoretical leakage limit on fin aspect ratios within two-fluid MECS devices with the help of finite element analysis.

High aspect ratio (AR) micro-channels can have very high surface area densities in excess of 5,000 m^2/m^3 where AR is defined as the ratio of channel width to channel height. System miniaturization is provided by the reduction in residence time (and consequent channel length) needed by fluid molecules flowing through micro-channel reactors and heat exchangers. Brooks [13], Wang [14], Peng [15], Friedrich and Kang [16] used the term surface area density to quantify this attribute of MECS devices defined as the amount of surface area per unit volume of device.

Further, the high AR micro-channels within MECS devices tend to have low pressure drops when compared with other high surface area density structures (e.g. sponges). In fact, the characteristic reduction in channel length causes MECS devices to have no theoretical increase in pressure drop over conventional systems. Overall, MECS devices provide the opportunity to greatly reduce the size and weight of energy and chemical system applications while providing the opportunity for enhanced process control for novel material synthesis.

Results from metallography and leakage testing performed by Dr. Brian Paul at Oregon State University revealed that for a given set of bonding conditions there exists a

maximum permissible value of aspect ratio (width/height of the cross-section of a channel) during bonding beyond which leakage is bound to occur. Furthermore, the results implied that higher aspect ratios can be achieved at smaller scales. Hence, the FEA model was used to determine these limiting values of aspect ratios for various laminae using *Abaqus CAE* to simulate the counter-flow device.
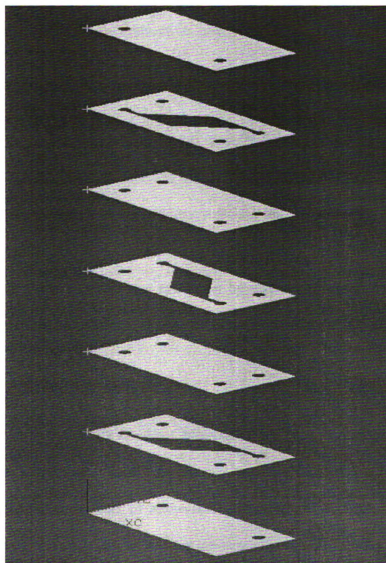
Figure 2: Exploded view of the FEA model of counter-flow micro-channel array investigated in this study

1.2 DESIGN AN ACTIVE COOLED AND EFFICIENT MESO-SCALE HEAT EXCHANGER USING A FUNCTIONALLY GRADIENT MATERIAL

Many researchers have attempted to remove heat from microelectronic devices. One of the more popular methods to dissipate the heat is to spread rapidly by employing highly conductive and high heat capacity materials such as diamond, silicon nitride, molybdenum, etc. [21, 22, 23]. Heat is dissipated to the environment either by forcing air through pin arrays or fins or by cooling naturally. Recently MEMS-sized heat exchangers have emerged which rely on convective heat transfer via air. In such cases, heat inevitably spreads to its surrounding and other peripheral devices.

More efficient cooling results when coolants circulated through networked channels and manifolds in a closed system. Bower and Mudawar [24] and Gillot [25] developed a two-phase heat exchanger with a higher efficiency. Bower and Mudawar [24] made mini and micro-channels on blocks made of copper and nickel plates. This work is an attempt to design an efficient active cooled heat exchanger by minimizing residual thermal stresses in the heat exchanger. To achieve this, we propose to the body of the heat exchanger to be micro-textured.

Micro-textured or Functionally Gradient Material (FGM) can be processed by spatially modulating the compositional ratio between two powders. Further, the body of the heat exchanger consists of a network of micro-scale channels and manifolds through which the coolant is transported. Applications for the heat exchanger include a variety of other industrial or medical uses, such as conduits for fluids in engines or to carry medicines or biological fluids.
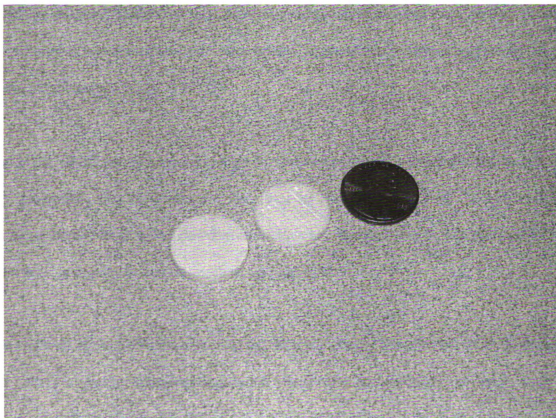
Figure 3: Photo of the Alumina-Zirconia FGM – one with internal channels and the other with external channels

Structural and thermal properties of FGMs can be tailored by spatially varying the composition of the second-phase particles in the matrix material. This is achieved by modulating the concentration level of the second phase during fabrication. Therefore, the FGM fabrication processes should possess the ability to produce various distributions of particles to withstand assigned loading.

Powder metallurgy is the most versatile and most popular method of fabricating a bulk FGM. The state of powder metallurgy technologies in fabricating FGM is reviewed by Watanabe and Kawasaki (1990). This process involves sintering of powder mixtures with

varying volume fractions of the constituent materials. One drawback behind powder metallurgy is that controlling the concentration levels of the constituent materials can be quite cumbersome.

An FGM ideally has continuous gradiency. One can approximate such gradient properties by preparing subcomponents in the form of layers. Each layer is prepared by homogeneously mixing two powders in various ratios, which can be stacked to form the 'discrete' gradiency in thermo-mechanical properties.

One area of micromechanics is concerned with calculating the effective or bulk physical properties of locally inhomogeneous, but statistically homogeneous, materials such as composite materials. Composite materials consist of at least two distinct phases – the matrix material and the reinforcing material, whose properties are known. Rather than microscopically modeling each inclusion in a composite medium, a given inhomogeneous material can be replaced by an equivalent "effective medium".

For our finite element analysis, alumina and zirconia were chosen for their inherent interfacial strength and difference in their coefficient of thermal expansion (CTE) values. The Mori-Tanaka (1973) approach was used to solve for the properties of the FGM as a function of the volume fraction of the particles or fibers.

Because of the almost similar sizes of the alumina and zirconia particles, the Mori-Tanaka mathematical model was solved twice-once for each of the two materials as the

matrix. It was found that the properties of the intermediate discrete layers were almost similar by using either of the two models. Hence, the average values were taken as the final material properties of the FGM.

In the micro-textured body of our heat exchanger with cooling channels, heat is conducted and dissipated via coolant circulating through the manifold channels (Fig 5). The novel processing techniques used to fabricate the heat exchanger involve:

(1)   Processing techniques to fabricate internal channels into an FGM by using a fugitive phase.

(2)   Powder processing techniques to produce the micro-textured heat exchanger undamaged by the process-induced stress.
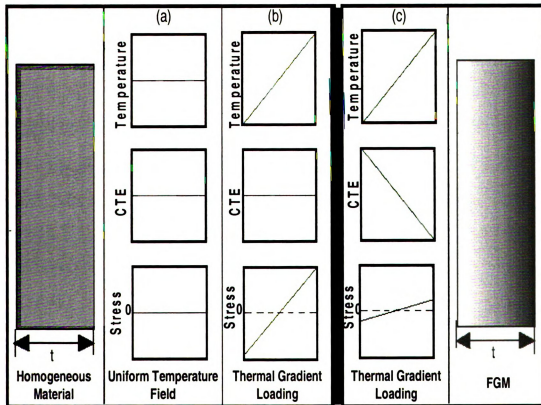
Figure 4: How FGMs work
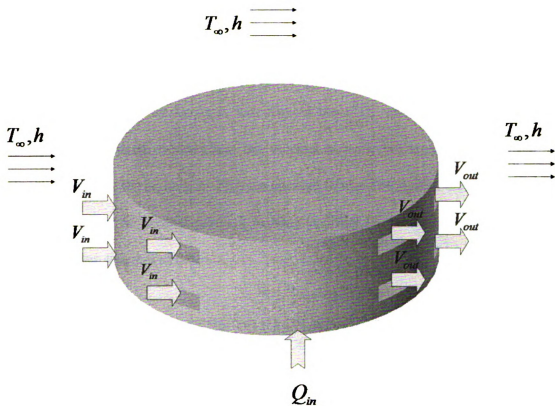
Figure 5: The heat exchanger with cooling channels (side view)
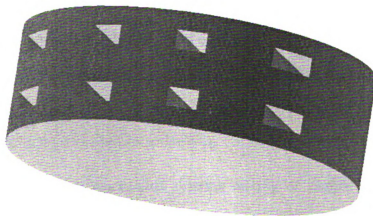
Figure 6: Front view of the heat exchanger showing 8 cooling channels

The key issue in producing micro-textured medium (FGMs) is to avoid damage due to process-induced residual stress. Residual stresses in FGMs [26, 27] occur due to spatial variations in Coefficient of Thermal Expansion (CTE) and densification behavior during processing. However, it is also this variation in the CTE values which is one of our design parameters used to minimize the thermal stresses because of a large thermal gradient. Hence, with the help of FEA an attempt is made to design the heat exchanger such that the effect of thermal gradient loading is offset by the variation of the CTE to give us minimum thermal stress.

1.3 DESIGN OF RIBBED DUCTS TO FACILITATE MIXING OF TWO LIQUIDS IN MICRO-FLUIDIC DEVICES

Rapid mixing is essential in many of the micro-fluidic systems targeted for use in the testing of biochip analysis, drug delivery, and analysis or synthesis of blood, among others. Mixing initiates many of these processes by rapidly increasing rates of enzyme reactions, cell activation or protein folding. Effective mixing is characterized by an increase in the contact area between the fluids and a decrease in the distance over which diffusion needs to act such that diffusion can complete the mixing process rapidly [28]. In macroscopic devices, turbulent three dimensional flow structures or mechanical actuators can be used to accomplish this.

However in micro electro mechanical systems mixing of sample and reagent fluids quickly is a major issue since the physics of fluids at these length scales precludes the normal available mechanisms for mixing. Mixing is dominated by molecular diffusion process in which the diffusion time is proportional to the square of the length scale.

However for a channel with dimensions of about 100 μm, the diffusion times are too slow to rely upon for effective mixing [29].

The difficulty in mixing fluids on the microscale lies in the size of the devices. Because of the small scales, these flows are predominantly laminar, so the efficient mixing obtained in turbulent flows is not practically attainable. While it is possible to design active micromixers that utilize macroscale mixing techniques such as mechanical stirring, the inclusion of active elements often leads to very complex and costly fabrication schemes. Turbulence occurs in flows characterized by high Reynolds number Re > 2000. For a characteristic velocity and length scale U, D and kinematic viscosity ν, Re is defined as: $Re = UD / \nu$

For typical dimensions of MEMS devices around 200 μm and assuming highest flow velocities to be around 100 mm/s, we have Re = 20. Typically Re is much lower in the 1-10 range and for creeping flows Re < 1. This flow regime severely precludes turbulence as a possible mechanism.

For planar devices, diffusion is limited by the in-plane dimension of the fluid channel. Using Fick's equation, the diffusion mixing time is defined by, $T_d = L^2 / \kappa$, where L is the characteristic mixing length, κ is the Fick's diffusion coefficient. For salt in water, κ = 1000 μm² / s, and using L = 200 μm, we find T_d = 40 seconds. Thus mixing times by diffusion are too slow for the viability of MEMS mixes in most applications [28].

Most designs of micromixers can be broadly classified as either active mixers or passive mixers. Active mixers are those that exert some form of active control over the flow field. They can usually do an excellent job of mixing. However they normally use electrokinetic or thermally actuated flow and actuators, valves and pumps which make them difficult to fabricate, operate and integrate into microfluidic systems. Passive micromixers utilize no energy input except for a pressure head to drive the flow. The key advantages that they offer are the simplicity in fabrication and operation and reduction in cost.

Partly due to the challenge of achieving high mixing rates in passive mixers, the literature contains significantly lesser number of designs of passive devices compared to active ones. Our goal has been to design a passive micromixer that allows fast mixing of small amounts of liquids. The ducts have inclined ribs or patterned grooves on all four walls which assist the mixing process by the vortex phenomenon of fluid stirring.

Most of the earlier computational studies on internal coolant passages have been two-dimensional. In recent years a number of three-dimensional studies have been reported. Three dimensional studies are needed on ducts with ribs, 180 degree bends, and/or rotation. Very few investigators performed computational studies on ducts with inclined ribs, which are used in advanced designs. When computing ducts with ribs, it is important for the geometry of the ribs to be captured correctly. This is because they exert considerable influence on the flow and heat transfer.
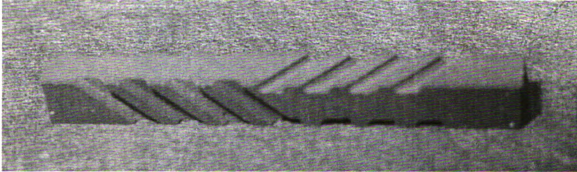
Figure 7: Photo of the ribbed duct
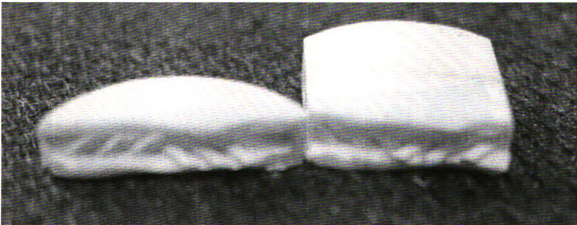
Figure 8: Cut-out photo of the internal ribbed ducts
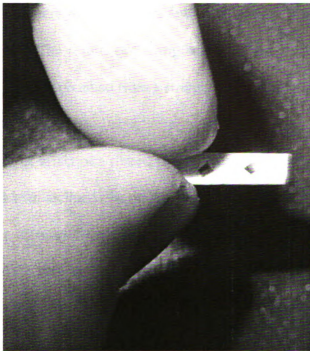
Figure 9: Photo of internal ribbed ducts

Figure 10: CFD model of the ribbed duct

The model was solved using Fluent 6.0, a commercial computational fluid dynamics code. Mixing conditions were simulated for a few combinations of liquids that are known to be almost immiscible. The results of mixing between these liquids in the ribbed duct were then compared to those obtained from a straight simple duct.

Shih, et al [3] studied the effect of a ribbed U-duct with or without rotation. Their model consisted of a U-duct with inclined ribs on just two opposite faced walls. They developed a mesh capturing the effects of the side ribs to perform computational fluid dynamics simulations. We used the code written by Shih et al [30] and modified it so that the mesh now represented our geometry.

Our geometry was a straight duct which consisted of two pairs inclined ribs, both being at an angle of 90 degrees to each other. Near the inlet the ribs were on the top and bottom sides of the duct, while near the outlet the inclined ribs were placed on the two opposite side walls. We came up with this design to ensure a more thorough mixing.

The code by Shih et al [30], which was in NASA plot3D format, was first converted to ASCII dat format readable by Gambit a CFD meshing tool. Then a code in C++ was written to modify the grid according to the required geometry. Later, the modified grid was imported into Gambit where the boundary conditions were applied. The same mesh was then used to simulate the flow and mixing in Fluent 6.0 for a few combinations of almost immiscible liquids.

2. FINITE ELEMENT ANALYSIS OF THE MICRO-LAMINATED HEAT EXCHANGER

This part of the thesis investigates the limits of fin aspect ratios within two-fluid counter-flow micro-channel arrays based on the minimum required stress state needed to laminate arrays by diffusion bonding. In the paper by Paul [20], it has been established that the diffusion bonding of two-fluid systems by micro-lamination can result in regions of the device that do not directly transmit bonding pressure and, consequently, result in unbonded regions leading to device leakage. A finite element model for analyzing the stress state in these unbonded regions was used to determine the minimum stress state necessary to adequately bond a given geometry. Model results were then compared with experimental results for a range of different counter-flow geometries. It has been found that under a given set of bonding conditions, a minimum stress state exists which must be met in every part of the geometry in order to produce leak-free bonds. Implications of this finding on the design of two-fluid micro-channel arrays were discussed. The experimental work was carried out by Dr. Brian Paul at the Oregon state university. The results of these findings were presented in Paul et al 2004 [39]. This chapter of the thesis has been adapted from the above research paper.

2.1 PROBLEM DEFINITION

For this investigation, the case of a two-fluid, counter-flow, micro-channel array was investigated though it is expected that the conclusions of this work will apply to other types of two-fluid micro-channel arrays. The counter-flow device is comprised of

alternating layers of micro-channels, which allow the two fluids to flow in opposite directions separated by fins. A concept of the lamina design for a micro-laminated two-fluid, interleaved, counter-flow micro-channel array is shown in Figure 2. It is assumed that once the laminae are stacked they are diffusion bonded according to Figure 2. The plan view of the resulting monolithic device comprised of micro-channels and fins is shown in Figure 11.

In order to diffusion bond the laminae, a uniform bonding pressure is applied on the stack at an elevated temperature. The pressure is transmitted uniformly through the device except at the neck of the micro-channel (where the cross-section AA is in Figure 11). The lack of bonding pressure causes the laminae to remain unbonded at points A & B resulting in leakage within the device and mixing of the two fluids.

Figure 11 shows a region where pressure was directly transmitted through all of the laminae and exhibits excellent bonding. Figure 12 shows a region where pressure was not transferred directly between adjacent laminae because of the counter-flow design [20]. Figure 12 exhibits unbonded regions.

By experience, the width of the channel has to be constrained to a dimension where bonding will occur. The limit on the width of the channel, at which bonding takes place, depends on the thickness of the lamina. In other words, as the thickness of the fin laminae above and below the neck of the micro-channels increases, the neck can be made wider.
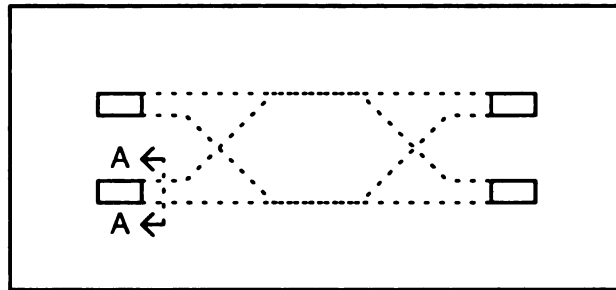
(a)
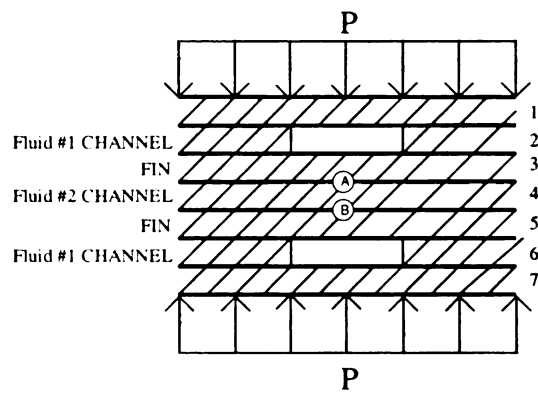
(b)

Figure 11: a) The plan view of the two-fluid interleaved, counter-flow micro-channel array comprised of micro-channel and fin laminae; and b) Cross-section of the device at cross-section A-A
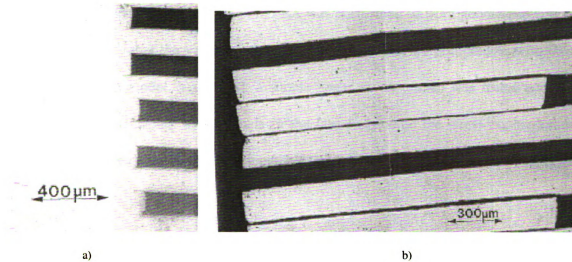
Figure 12: Cross-section of a diffusion-bonded counter-flow micro-channel heat exchanger showing sections through which the bonding pressure: a) was transmitted; and b) was not transmitted. Cross-section b resulted in leakage between the two fluids (Courtesy Dr. Brian Paul, Oregon State University)

The ratio of the channel span in the neck region to the fin lamina thickness is the fin aspect ratio. It is expected that for a given set of bonding conditions (time, temperature, bonding pressure), there will exist a critical minimum pressure that all areas of the laminae must receive in order to bond. This minimum pressure will ultimately constrain the fin aspect ratio for any given two-fluid micro-channel device.

2.2 FINITE ELEMENT MODEL

An analytical approach to modeling this phenomenon has been attempted based on simple elastic beam theory [20]. However, no generalizable conclusions were gained. Here a finite element model is used to analyze the effect of changing lamina thicknesses and channel (neck) widths.

To simplify the modeling of this phenomenon, a test coupon was developed (Figure 13) to approximate the conditions of the necked region shown in Figures 11 (a) and (b). To

validate the geometry of the test coupon, FEA was performed on both geometries (Figure 2 and 13) to verify that the values of the out of plane stresses are comparable with those in the test coupon model. To do this, a simple linear elastic model was found adequate since it is recognized that the channels in the lamina become the stress concentration. The two geometries were found be comparable across a wide range of channel widths and fin thicknesses.

For the analysis, certain assumptions were made. The 6-layered test coupon used was assumed to be 25.4 X 25.4 mm in width and breadth with varying thickness depending on lamina thickness, h. Critical dimensions of the first and third laminae in the test coupon are shown in Figure 13 (b) including the span (width) of the channel, a. As the model was always under compression, to reduce contact non-linearity problems, the analysis was performed on a $6h$ thick 3D deformable model instead of 6 separate layers each with thickness h. Two rigid three-dimensional discrete plates were used on the top and bottom to apply the bonding pressure.

The model was a linearly elastic isotropic model with the following material properties: E = 124,800 N/mm^2, υ = 0.2235. These values were chosen as the respective elastic properties at the temperature where diffusion bonding of the lamina took place.
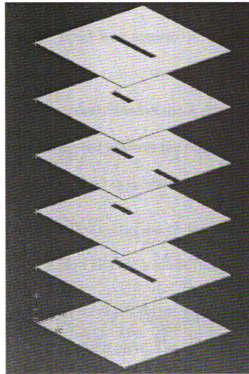
(a)
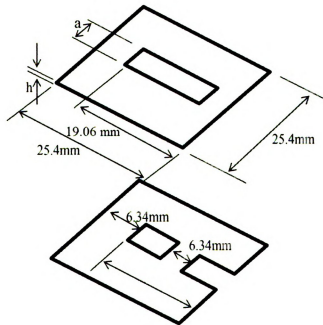
(b)

Figure 13 (a) Geometry of the test coupon studied in this paper and verified by leakage testing. (b) Specific critical dimensions of the test article used in this study

Contact was defined between the rigid plates and the set of the deformable plates representing the heat exchanger. Load was applied in 3 steps to prevent numerical singularity:

(1) The deformable body was constrained in the Z direction. Then the top & bottom rigid plates were moved towards the body of the heat exchanger by a very small distance (1 e-08 mm) to establish the contact between the nodes.

(2) After removing the Z direction constraint on the deformable body the bottom rigid plate was constrained in all 6 degrees of freedom.

(3) After removing the displacement BC on the top rigid plate, a pressure of 5.86 MPa was applied on the top rigid plate. The load was applied in steps of 100 to prevent numerical singularity and negative eigenvalue.

An 8-noded brick element with reduced integration (C3D8R) was used for all the models. For the rigid plates, 3D rigid elements were used. FEA was performed for the following values of thickness of the lamina plates: 76.2 μm, 152.4 μm, 203.2 μm, 254 μm, and 508 μm. For each of these values of thickness, a range of channel spans were chosen and FEA was used to predict the limiting value of the channel span to avoid leakage. As shown in figure 12, the leakage problem occurs in the neck region of the channels of the heat exchanger model and on the third layer from the top of the test coupons. Thus, the critical stress is defined as the out-of-plane nodal stresses (S33) on the "bridge region" of the layer 3, i.e. the region on layer 3 between the channel and the slot on the right. The stress contour images [Figure 14, 15, 16(a) and 16(B)] in this thesis are presented in color.
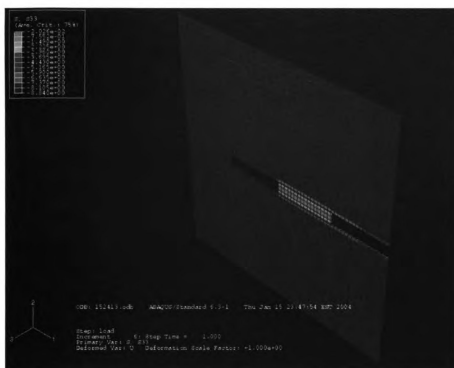
Figure 14: S33 stress contours on test coupon with h = 152.4 μm and a =1.3mm
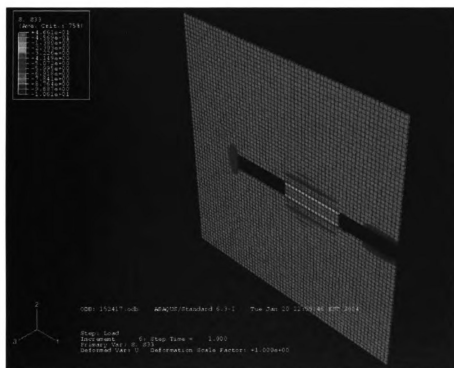
Figure 15: S33 stress contours on test coupon with h = 152.4 μm and a =1.7mm
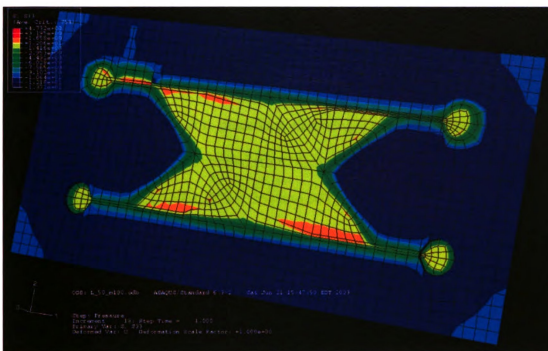
(a)
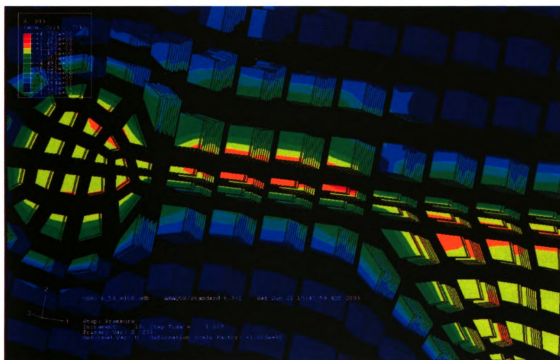
(b)

Figure 16: (a) S33 stress contours from FEA on counterflow microchannel model (h = 152.4 μm and a =1.7mm). (b) Zoomed in view

2.3 EXPERIMENTAL APPROACH

All experimental work was done by Dr. Brian Paul's research group at Oregon State University. The fabrication procedure for making the test specimens (Figure 13 (a)) consisted of a micro-lamination procedure involving laser machining and diffusion bonding. First, laminae were patterned from blanks of 304 stainless steel shim stock of various thicknesses (76.2, 152.4, 203.2, 254 and 508 μm) using a 532 nm Nd: YAG laser installed on a laser micromachining system. Overall size of the laminae was 25.4 x 25.4 mm. Critical dimensions of the first and third laminae are shown in Figure 13 (b). Efforts were made to remove laser burrs by abrasion after laser machining. Laminae were cleaned with an acetone, methanol and DI water for degrease and rinse and put into an alignment fixture to be bonded in a vacuum hot press. The base of the hot press fixture was made of graphite with tungsten pins for facilitating the edge alignment of the laminae. All laminae were diffusion bonded in the vacuum hot press at 900° C and 5.86 MPa for 2 hours.

Preliminarily, a set of test coupons were developed to verify the existence of the bonding problem under study. Laminae thicknesses for preliminary coupons were 254 μm and 508 μm. Metallography was conducted on these coupons to verify bonding conditions. Once the process was verified, additional test specimen were produced in the remaining lamina thicknesses. To speed up testing, the bonds of these devices were evaluated by means of a leakage test in which the open header was pressurized by air to several atmospheres and held under water to look for air leakage.

2.4 RESULTS

To begin the experimentation, three specimens of 508 μm thick SS with channel spans of 2.54 mm, 3.175 mm, and 5.08 mm were diffusion bonded at the conditions described previously. Metallography of the specimens revealed that the specimens with 2.54 mm and 3.175 mm spans were bonded below and above the channel, whereas small gaps between laminae were detected for the specimen with the 5.08 mm span. Figure 17 represents the micrographs of the 508 μm thick specimens.
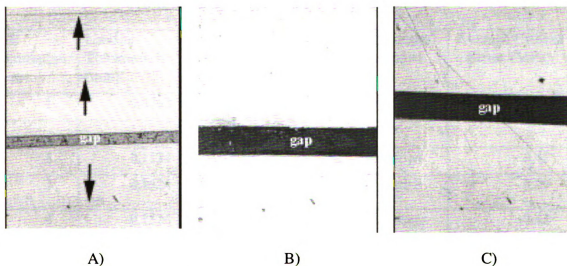
Figure 17: Micrographs of test specimens consisting of 508 μm thick laminae: A) 5.08 mm SPAN (50X); B) 3.175 mm SPAN (50X), AND C) 2.54 mm SPAN (50X). (Courtesy Dr. Brian Paul, Oregon State University)

Similarly, three specimens of 254 μm device with a channel span of 1.524 mm, 2.54 mm, and 5.08 mm were diffusion bonded. Metallography of the specimens showed that specimens comprised of 5.08 mm and 2.54 mm were not bonded above and below the channel span, whereas the specimen with 1.524 mm thick laminae did not have any gaps.

Micrographs of these specimens are shown in Figure 17. Further experiments were performed by fabricating and leakage testing specimens consisting of 76.2 μm, 152.4 μm, and 203.2 μm thick laminae. A summary of results from the FEA model is shown in Table1. These results also compared well both with the metallography and leakage tests. The values displayed in Table 1 are the averaged critical stress values that were obtained after averaging all the nodal out-of-plane stress in this *bridge region*.

Table 1: The Geometrical Specifications of All Test Coupons and the Results of FE Simulations for Average Critical Stresses

FE simulation Case	Lamina Thickness, h (mm)	Channel Span, a (mm)	Aspect Ratio, a/h	Leakage/ Bonded	Average Critical Stress (MPa)
1	0.0762	0.75	9.84	Bonded	- 0.17
2	0.1524	0.50	3.28	Bonded	- 0.45
3	0.1524	1.30	8.53	Bonded	- 0.05
4	0.1524	1.70	11.15	Leakage	+0.43
5	0.1524	2.50	16.4	Leakage	+0.44
6	0.2032	1.0	4.92	Bonded	- 0.30
7	0.2032	1.5	7.38	Bonded	- 0.07 to + 0.1
8	0.2032	2.2	10.83	Leakage	+ 0.45
9	0.2032	3.5	17.22	Leakage	+ 0.39
10	0.254	1.8	7.09	Bonded	- 0.05 to + 0.15
11	0.254	2.6	10.24	Leakage	+ 0.36
12	0.508	3.1	6.1	Bonded	- 0.026 to + 0.15
13	0.508	5.1	10.04	Leakage	+ 0.30

For most cases, the value of critical stress is almost constant throughout the bridge region. However for a few cases (Cases 7, 10 and 12 in Table 1), we see that this value is not constant unlike other cases. There is a slight variation in the stresses showing some nodes being in tension and other nodes being in compression. For example, the variation in stress for Case 10 ranges from -0.05 to 0.15MPa.

The stress contours in Figures 16 (a) show the out-of-plane stress (S33) distribution on the heat exchanger model for h = 0.1524 mm and a = 1.70 mm. Figure 16 (b) is a zoomed in view of one of the channels of the same model. Figures 14 and 15 are S33 stress contour plots on the test coupon for the same h = 0.1524 mm but different channel spans. We see that the stresses for the same model (h = 0.1524 mm and a = 1.70 mm) on the heat exchanger model and the test coupon are comparable.

2.5 DISCUSSION

From the FEA model we can predict that when the value of the S33 critical stress reaches + 0.2 MPa, then leakage takes place. Also when there are a few nodes in the *bridge region* in tension and a few in compression, and when the value of the tensile stress on these nodes does not exceed + 0.2 MPa then the layers are just bonded. However, we can safely say that the layers will be bonded together when the stresses present in the *bridge region* are purely compressive. The results of the FE simulation show that simple elastic FE models with a set of lamina thickness and channel span without modeling the complex creep behavior of the lamina allow you to determine the interfacial stress between the lamina. Based on the sign of the stress, we can evaluate if diffusion bonding can take place or not.
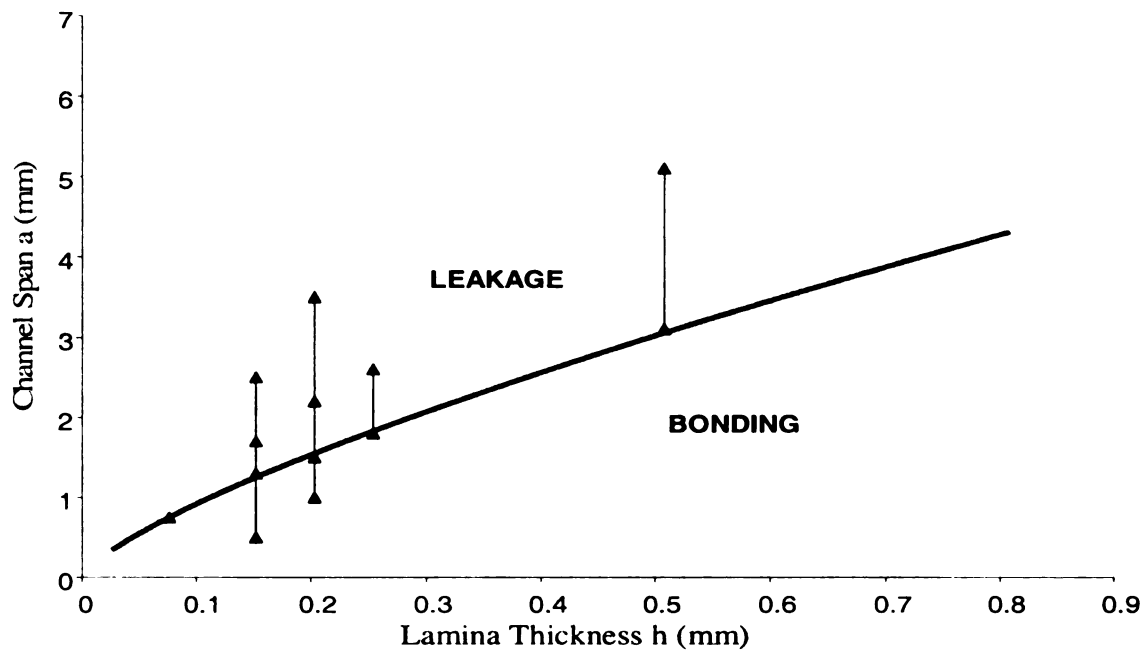
Figure 18: A plot of the experimental results showing the conditions under which bonding and leakage occurred. Bonding conditions for all of these samples were 5.86 MPa at 900°c for two hours
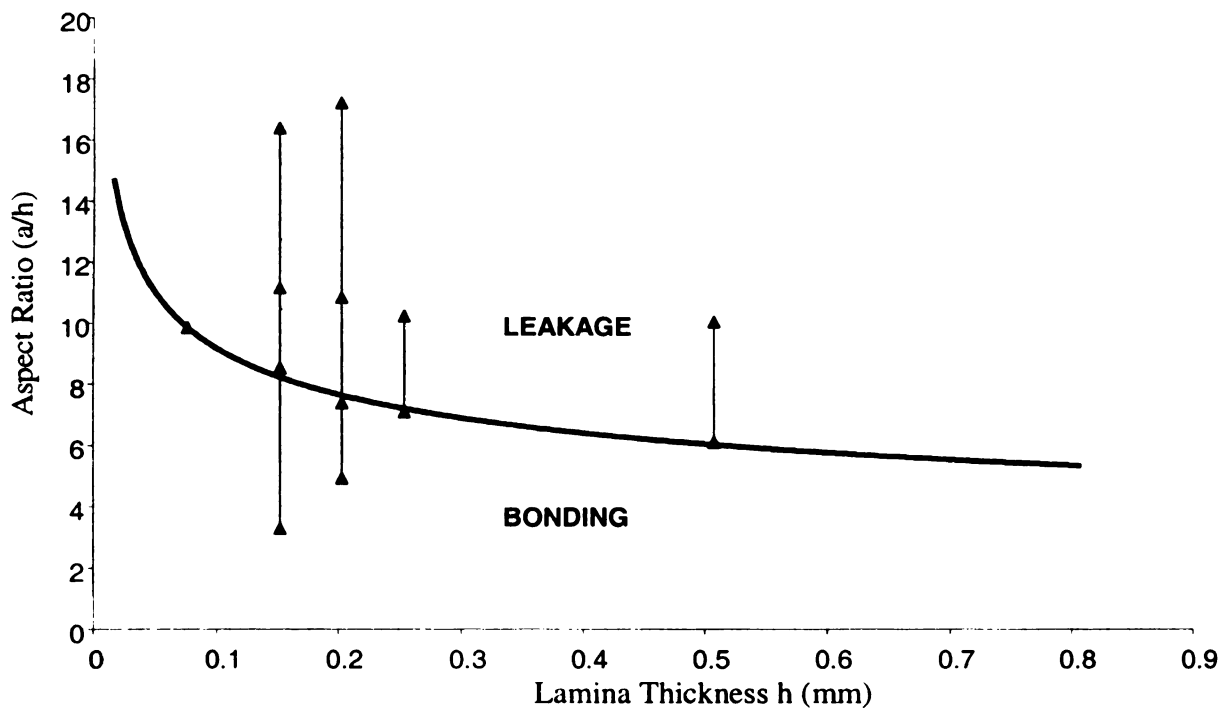
Figure 19: A plot of the experimental results showing lamina thickness Vs aspect ratio

2.6 CONCLUSIONS

An investigation on limits of aspect ratio for counter-flow heat exchangers was carried out in this study. The simulation results were verified by carrying out the leak tests on test coupons. Following are the conclusions of this study:

1. The fins in two-fluid micro channel heat exchangers have a certain aspect ratio limit for a certain given thickness of the lamina, beyond which poor bonding will occur within the device resulting in leakage and mixing of the two fluids in the device.

2. For a given set of bonding conditions, the width of the channel can be interpreted as a function of the thickness of the lamina with the key bonding characteristic being that only compressive out of plane stresses exist in the critical neck region. It is expected that the laminae may just bond even if a tensile stress up to a maximum of 0.15 MPa exists in few places in the critical neck region, provided that on all the other places of the neck region the out-of plane stress is purely compressive.

3. It is expected that higher aspect ratios can be accommodated at smaller scales with high aspect ratio (greater than 30) fins possible at lamina thicknesses less than 1.36 μm for this set of bonding conditions.

3. FINITE ELEMENT ANALYSIS OF A OF FUNCTIONALLY GRADIENT MESO-SCALE HEAT EXCHANGER

The miniaturization of electronic components and the rapid increase in power density of advanced microprocessors and electronic components have created a need for improved cooling technologies to achieve high heat dissipation rates. Some of future microprocessors and power-electronic components have been projected to dissipate over 1000 W/cm2. The traditional methods of electronic cooling such as conduction and natural/forced convection have proved to be insufficient for such high heat fluxes. The need for new technologies capable of dissipating high heat fluxes and requiring low input power is of critical importance to many industries. Coupled with these are requirements of low volume/weight addition, high portability, high reliability and large-scale fabricability of such future cooling devices.

The cooling system explored in this project was the fluid flow through an array of parallel micro-channels. Among the advantages of this cooling method is the closeness of the micro-channels to the heat source and therefore the thermal resistance is reduced. Among the disadvantages is the non-uniform variation of heat flux throughout the body of the heat exchanger. This in turn causes uneven expansion which results in high induced thermal strains, warping and even cracks. We propose to use Functionally Gradient Materials to offset this effect of thermal gradient loading.

3.1 BACKGROUND

A key issue we face in our design is to distribute these FGM layers such that the thermal strains are minimized. Considering the case of a long rod with a linear CTE, the change in length due to temperature change is given by:

$$\Delta l = l\alpha\Delta t$$

where,

l = length of the rod

Δl = change in length due to change in temperature (heating or cooling)

α = coefficient of thermal expansion of the material of the rod

Δt = change in temperature of the rod

Hence the induced thermal strain along the length of the rod is given by:

$$\varepsilon = \frac{\Delta l}{l} = \alpha\Delta t$$

In our case, the bottom surface of the device is subjected to a high heat flux [Fig. 5]. Now if the whole device is made up of the same material, then the part very near the high heat flux part tends to expand more than the rest of the body. Hence the objective is to build the device using FGMs such that the layer closest to the heat flux has the least coefficient of expansion. Alumina and Zirconia powders were used to make the FGM. Because of the almost similar sizes of the alumina and zirconia particles, the Mori-Tanaka mathematical scheme was solved once for each of the two as the matrix material. The average values were taken as the final material properties of the FGM.

3.2 FUNCTIONALLY GRADIENT MATERIALS

The unique feature of the heat exchanger is network of channels and manifolds in the micro-textured medium achieved by spatially varying the compositional ratio between two powders during conventional and microwave powder processing. The micro-textured medium is necessary to compensate thermal gradient loading as a result of heat transfer into a cooling fluid circulating in the network of channels and manifolds. The residual stress, induced by spatial variations in properties and densification, is minimized by using different powder characteristics. The fugitive phase in the shape of desired channels is used during compaction, which decomposes during sintering leaving cooling channels.

A key issue in producing functionally gradient materials is to avoid damage due to process-induced residual stress. Residual stresses in FGMs [27] occur due to:

(i)   Differential shrinkage in between the co-sintering layers due to their different sintering kinetics during processing (densification behavior)

(ii)   Thermal expansion mismatch

In order to resolve this problem the difference in the two shrinkage mechanisms existing in powder processing must be utilized, namely the effect of CTE and densification behavior. During densification, the interstitial spaces among the powder are filled due to mass transport mechanisms. The shrinkage differences due to CTE mismatch are intrinsic for a given combination of materials after consolidation. However, the shrinkage from the densification of powder can be altered by designing the powder characteristics and optimizing the sintering conditions such as time, temperature, heating/cooling cycles, etc [31].

The starting powder characteristics and sintering conditions can compensate for the CTE difference by exploiting the differences in densification behavior among the layers. Powder shrinkage during densification must be understood as a function of various processing variables such as the powder characteristics as well as sintering conditions. The powder characteristics influence the initial powder packing density which in turn affects the densification behavior during sintering. Methods to control the initial powder packing include mixing a few batches of powders with different average particle sizes [32].

3.3 MORI-TANAKA SCHEME

Rather than microscopically modeling each inclusion in a composite medium, a given inhomogeneous material can be replaced by an equivalent "effective medium". Its effective properties can be determined by applying the appropriate homogeneous boundary condition with physical properties of the constituent materials. In particular, the Mori-Tanaka theory [33] may be used for this purpose. Under the assumption of Mori-Tanaka, the effective stiffness tensor is,

$$C^* = C^{MT} = C_m + v < (C_f - C_m)A^{MT} >$$

where,

v = represents the volume fraction of particles or fibers

C_m = stiffness tensor of the matrix material

C_f = stiffness tensor of the particle (fiber) material

A^{MT} = strain concentrator

The bracket < > represents orientation distribution function (ODF) – weighted orientational averaging. ODE – weighted averaging for anisotropic and ellipsoidal inclusions was extensively discussed by Ferrari and Johnson (1989). Limitations on the applicability of the Mori-Tanaka theory have been discussed by Ferrari (1991). For the FGM body made of isotropic matrix and isotropic spherical inclusions, both the Mori-Tanaka and the poly-inclusion method predict the effective stiffness to be

$$C^* = C^{MT} = C_m + v(C_f - C_m)A^{MT}$$

Here, the strain concentrator, A^{MT}, is defined as

$$A^{MT} = T[(1-v)I + vT]^{-1}$$

where,

I = fourth-rank identity tensor

T = Wu's tensor

Wu's tensor (1966), is defined as

$$T = [I + ES_m(C_f - C_m)]^{-1}$$

where,

E = Eshelby tensor

S_m = Compliance tensor of the matrix material

The Eshelby's tensor for spherical inclusions written in 6 X 6 matrix form is

$$[E] = \begin{bmatrix} \dfrac{7-5\nu}{15(1-\nu)} & \dfrac{5\nu-1}{15(1-\nu)} & \dfrac{5\nu-1}{15(1-\nu)} & 0 & 0 & 0 \\[3mm] \dfrac{5\nu-1}{15(1-\nu)} & \dfrac{7-5\nu}{15(1-\nu)} & \dfrac{5\nu-1}{15(1-\nu)} & 0 & 0 & 0 \\[3mm] \dfrac{5\nu-1}{15(1-\nu)} & \dfrac{5\nu-1}{15(1-\nu)} & \dfrac{7-5\nu}{15(1-\nu)} & 0 & 0 & 0 \\[3mm] 0 & 0 & 0 & \dfrac{4-5\nu}{15(1-\nu)} & 0 & 0 \\[3mm] 0 & 0 & 0 & 0 & \dfrac{4-5\nu}{15(1-\nu)} & 0 \\[3mm] 0 & 0 & 0 & 0 & 0 & \dfrac{4-5\nu}{15(1-\nu)} \end{bmatrix}$$

where,

ν = Poisson's ratio of the matrix material

The stiffness tensors (C_m, C_f) are defined as,

$$[C_{ij}] = \begin{bmatrix} C_{11} & C_{12} & C_{12} & 0 & 0 & 0 \\ C_{12} & C_{11} & C_{12} & 0 & 0 & 0 \\ C_{12} & C_{12} & C_{11} & 0 & 0 & 0 \\ 0 & 0 & 0 & C_{11}-C_{12}/2 & 0 & 0 \\ 0 & 0 & 0 & 0 & C_{11}-C_{12}/2 & 0 \\ 0 & 0 & 0 & 0 & 0 & C_{11}-C_{12}/2 \end{bmatrix}$$

where C_{11} and C_{12} are related to Lame's constants defined as,

$C_{11} = \lambda + 2\mu$

$C_{12} = \lambda$

and where λ and μ are related to Young's modulus (Y) and Poisson's ratio (ν),

$\lambda = E\nu/\{(1+\nu)(1-2\nu)\}$, and,

$$2\mu = E/(1 + \nu)$$

In the Mori-Tanaka scheme, the effective compliance tensor, S^{MT}, may be obtained as the reciprocal of C^{MT} [34].

For thermal gradient applications, the effective thermal expansion coefficient (CTE) tensor, α^{*}, is required. The CTE corresponding to the Mori-Tanaka approach is

$$\alpha^{*} = \alpha_{m} + (\alpha_{f} - \alpha_{m})(S_{f} - S_{m})^{-1}(S^{MT} - S_{m})$$

In the above equation,

α_{m} = CTE of the matrix material

α_{f} = CTE of the particle material

S_{m} = Compliance tensor of the matrix material

S_{f} = Compliance tensor of the particle material

S^{MT} = The effective compliance tensor

For steady-state thermal conduction, the expression for the effective thermal conductivity for the composite spheres assemblage (CSA) model was obtained by

$$K^{*} = K_{m} + v(K_{f} - K_{m})A^{MT}$$

where,

K_{m} = Thermal conductivity of the matrix material

K_{f} = Thermal conductivity of the particle material

v   = Volume fraction of particles or fibers

A^{MT} = Strain concentrator

The specific heat of a specimen at temperatures below ambient temperature can be measured by a dynamic heating method. It has been found that except for the specific heat at 88K, those measured are close to the value predicted by the law of mixtures, i.e.

$$C = V_m C_m + V_f C_f$$

where,

V_m = Volume fraction of the matrix phase

V_f = Volume fraction of the particle phase

C_m = Specific heat of the matrix material

C_f = Specific heat of the particle material

Density of a material at a constant temperature can again be predicted by the law of mixtures, i.e.

$$\rho = V_m \rho_m + V_f \rho_f$$

where,

ρ_m = Specific heat of the matrix material

ρ_f = Specific heat of the particle material

The powders used to model our FGM, were alumina and Partially Stabilized Zirconia (PSZ). Two-layer (alumina and PSZ) have been successfully made [35] in the past. The first layer was made with the alumina powder designated TM-DAR, manufactured by

Taimai Co. Japan. The second layer was formed with a mixture of 30% CERAC, a kind of Fully Stabilized Zirconia (FSZ), and 70% PSZ (TZ-3YS).

Using the above relations, the material properties of the composites with varying volume fractions of TM-DAR alumina and TZ-3YS partially stabilized zirconia were determined. *Matlab* was used to solve the matrices in the above equations [Appendix A]. Because of the similar sizes of the two particles, the equations were solved once taking almunia as the matrix phase and then taking PSZ as the matrix. Table 2 gives the material properties of the two samples.

Table 2. Material property values of alumina and yttria-partially stabilized zirconia

Property	Alumina	Y-PSZ
Density (g/cc)	3.97	6.02
CTE (/°C)	8.1×10^{-6}	10.3×10^{-6}
Young's modulus (GPa)	350	200
Poisson's ratio	0.23	0.3
Thermal conductivity (W/m/K)	20	3
Specific Heat (J/Kg/K)	750	450
Flexural Strength (MPa)	355	660

3.4 DESCRIPTION OF DEVICE

The geometry of the proposed device is as shown in Figures 5 and 6. This device is primarily meant to cool electronic chips or cutting tools. It is subjected to a high value of heat flux on its bottom surface. The primary means of cooling this heat exchanger is through liquid coolants flowing through internal channels in the device. The device also

looses heat to the ambient air through convection from its side walls and its top surface. A flux of 250,000 W/m² enters through its bottom surface. The coolant used was water and step-wise varying linear properties with temperature were assumed.

Water flows in all four channels with an inlet velocity of 0.5 m/s along the length of the channels. The water is discharged at the outlet to the ambient at atmospheric pressure. The ambient air is assumed to be at 25°C and its convective heat transfer coefficient is approximated to be 60 W/ m² /K. The objective is to prevent solid temperatures from raising over 50°C. At the same time we also want to minimize the induced thermal strain in the body. As discussed earlier, the material of the lowest layer and the one nearest to the heat source should have the least CTE value. An attempt was made to study the values of thermal strains for different ratios of thicknesses of the FGM layers for a three layered model [Figure 20].
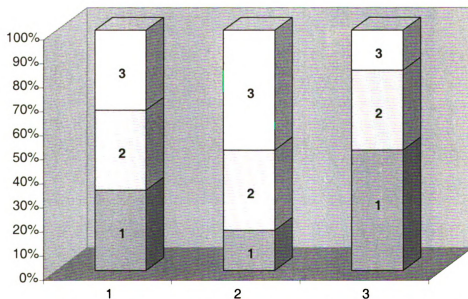
Figure 20: Different layer thickness ratios for a three-layered FGM model (Equal thickness layer model, Model 1 and Model 2)

For the three layered model, the bottom layer (layer 1) was alumina, followed by a mixture of 50% alumina and 50% zirconia (layer 2), and finally a layer of pure zirconia (layer 3). The combination with the least induced thermal stress was chosen. Then, the FEA simulation was repeated for a six-layered FGM model with again the design objective being to choose the one with the least induced thermal stress. The bottom layer is named layer one and the top layer is layer six. Again the six-layered model was built proportionately as follows:

Layer 1: 100% alumina

Layer 2: 80% alumina + 20% zirconia

Layer 3: 60% alumina + 40% zirconia

Layer 4: 40% alumina + 60% zirconia

Layer 5: 20% alumina + 80% zirconia

Layer 6: 100% zirconia
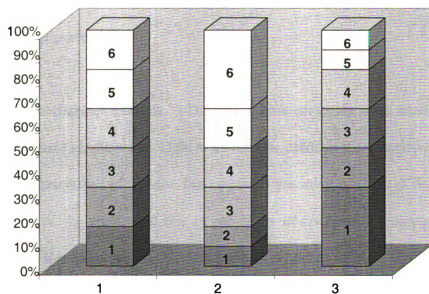
Figure 21: Different layer thickness ratios for a six-layered FGM model (Equal thickness layer model, Model 1 and Model 2)

The properties of the three and six layered FGM, solved from the Mori-Tanaka model, are tabulated in Appendix C.

3.5 FINITE ELEMENT MODEL

Our objective here is two-fold:

i. Solve the fluid-thermal interactions for temperature distributions in the FGM model as well as in the cooling fluid.

ii. Solve the thermal-structure interactions in the solid part for induced thermal strains.

We made use of *Ansys Multiphysics* to solve these coupled fluid-thermal-structure interactions. Care was taken to use only three-dimensional brick elements to mesh our models especially when computing flow through ducts. This is because it is important to align the grids along the direction of flow as they exert considerable influence on the flow and heat transfer.

For the fluid-thermal analysis, 3-D CFD flotran elements were used. The segregated solver was used for flow and TDMA solver was used for the velocity calculations. Here the thermal properties of the non-fluid material are several orders of magnitude different from those of the fluid, and this is called an *ill-conditioned conjugate heat transfer problem*. In this situation, the TDMA method probably will not yield useful results, no matter how many sweeps we specify. The most robust but most memory-intensive method for solving conjugate heat transfer problems, the Preconditioned Generalized

Minimum Residual method, was used as the temperature solver. Preconditioned Conjugate Residual method was chosen was the pressure solver because of its robustness for solving ill-conditioned heat transfer problems. Appropriate boundary conditions were applied (Figure 5) and the model was solved till desired convergence was achieved. Now the 3-D CFD flotran elements were replaced with 3-D structure elements in the solid regions, while null element was used in the fluid part. Then temperature boundary conditions were applied by importing the results file from the previous fluid-thermal analysis. Now the system was solved for thermal strains only in the solid regions. The analyses were performed on all the models of the three layered as well as six layered specimen.

3.6 RESULTS AND DISCUSSION

The results that were obtained from the finite element analysis were in agreement with our expected design objectives. First, the analysis was carried out on an alumina model and then the results were compared with the three layered and the six layered model.

3.6.1 Alumina model

Without the cooling channels, it was observed that the steady state temperatures were in the range of 280 °C to 250 °C. With the cooling channels we could bring down the steady state solid temperature range to 118 °C to 59 °C [Figure 22]. After the thermal-fluid analysis, a structural analysis was performed to determine the maximum principal stresses in the model [Figure 25 and 26]. It was observed that in the regions of high temperature gradients, the stress was the highest. These images in this thesis are presented in color.
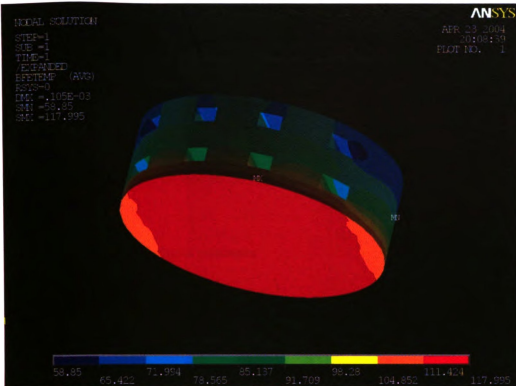
Figure 22: Temperature contours of the 8 -channeled alumina model
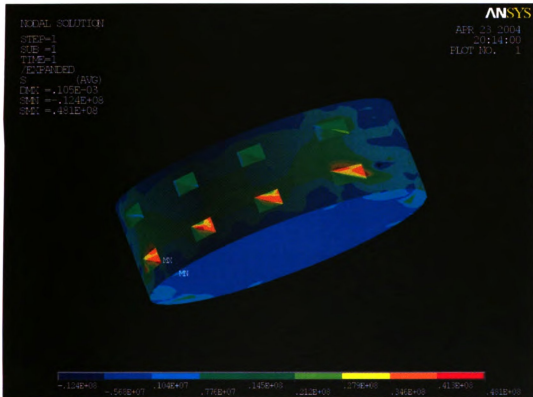
Figure 23: Maximum principal stress contours on the 8 -channeled alumina model

3.6.2 Comparing Results between – pure alumina, 3 layered FGM and 6 layered FGM

On comparing the results from the three models, it was found that the stress was least in the six layered FGM model, followed by the three layered model and it was maximum in the pure alumina model. Also for the models with the same number of layers, the ones with the smallest first layers produced the minimum stresses.

3.6.3 Maximum principal stress contours
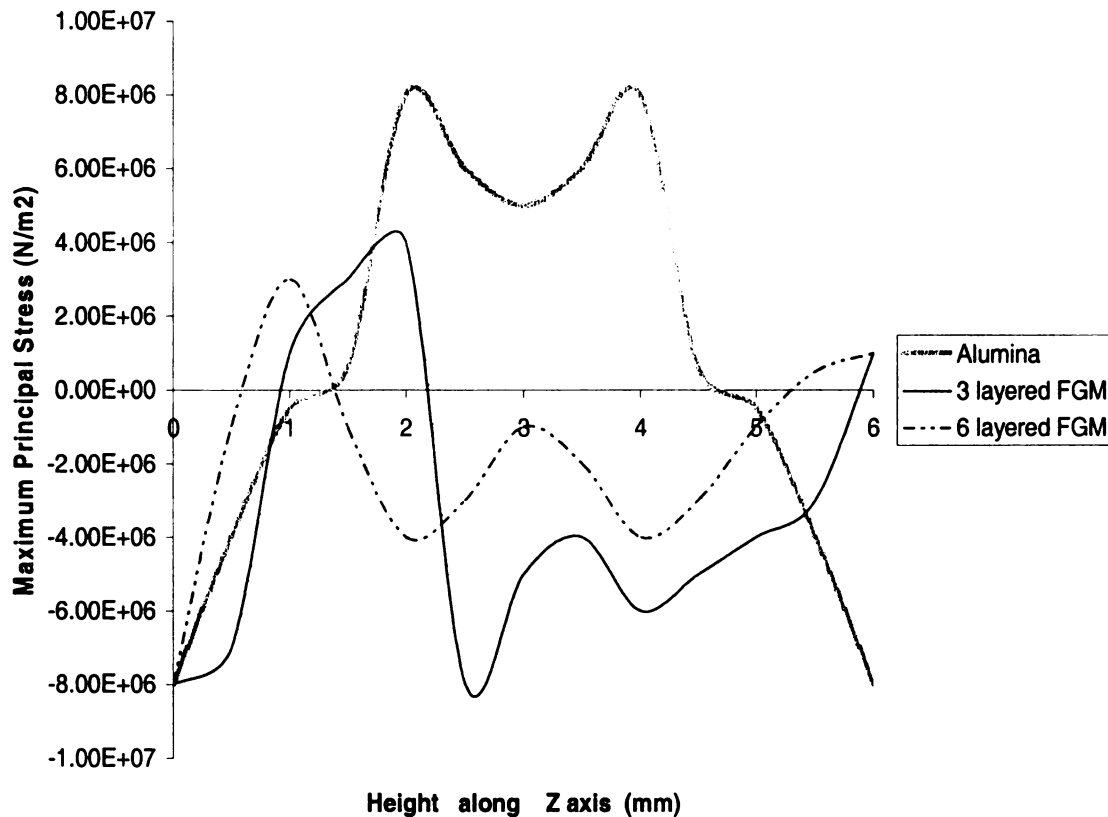
Figure 24: Maximum principal stresses at x = 0, y= 0

(FGMs have equal layer thickness)
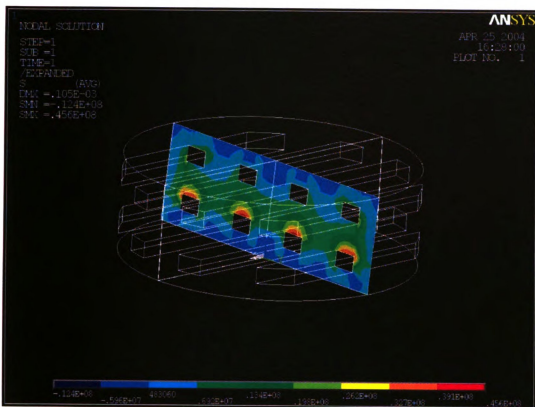
Figure 25: Alumina model - maximum principal stress contours at x=0
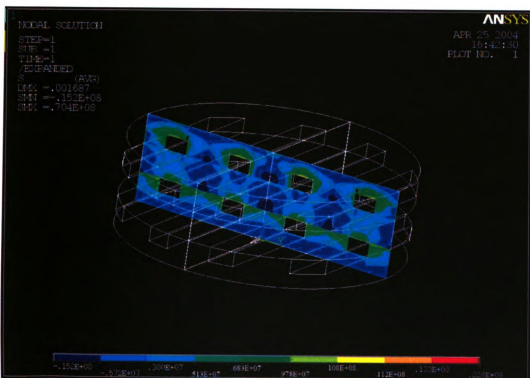
Figure 26: Three equi-layered FGM model - maximum principal stress contours at x=0
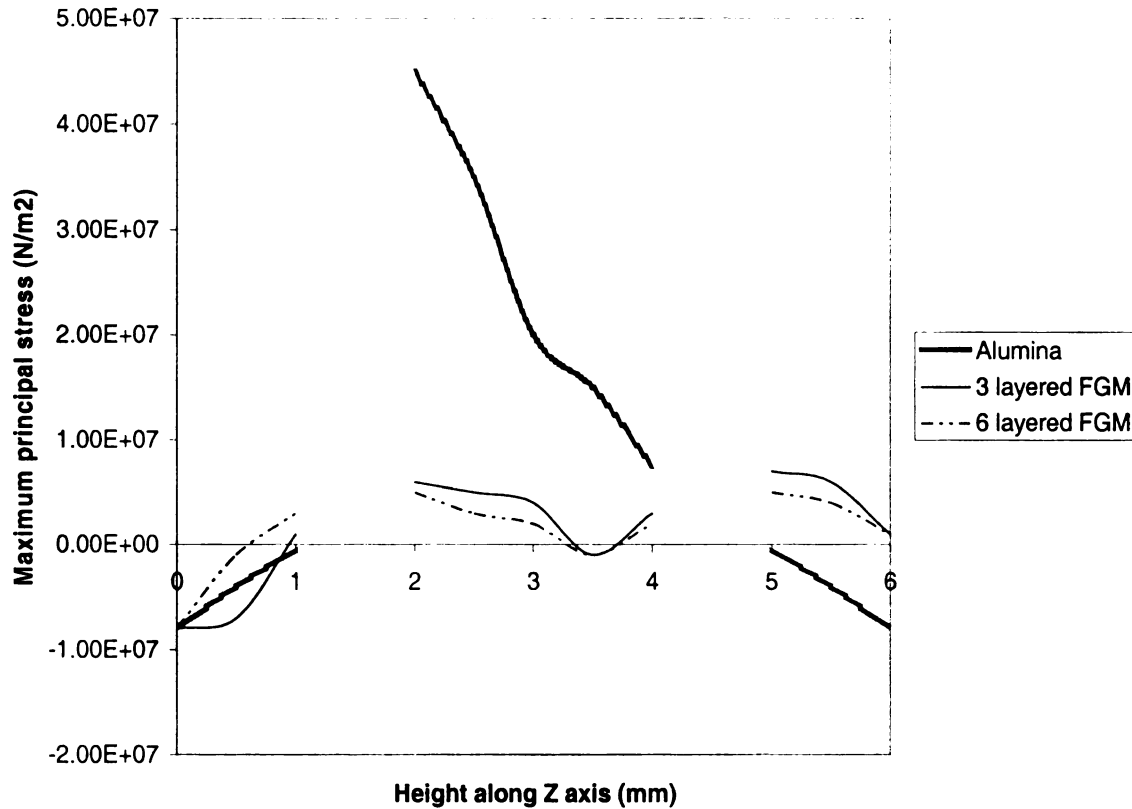
Figure 27: Maximum principal stresses at x = 0, y = 3mm
(FGMs have equal layer thickness)

From the above results it was seen that by building models using functionally gradient

materials, we succeeded in reducing the tensile stresses by almost half. Now, each of the

two FGM models – the three layered and the six layered, were analyzed to see the effect

in stresses by varying the thickness of each layer. The effect was not as pronounced as

seen between an alumina model and a FGM model. However the effect was seen more in

the case of the three layered FGM than the six layered FGM. For both the cases, the

models with the smallest first layers (model 1) produced the minimum principal stresses.
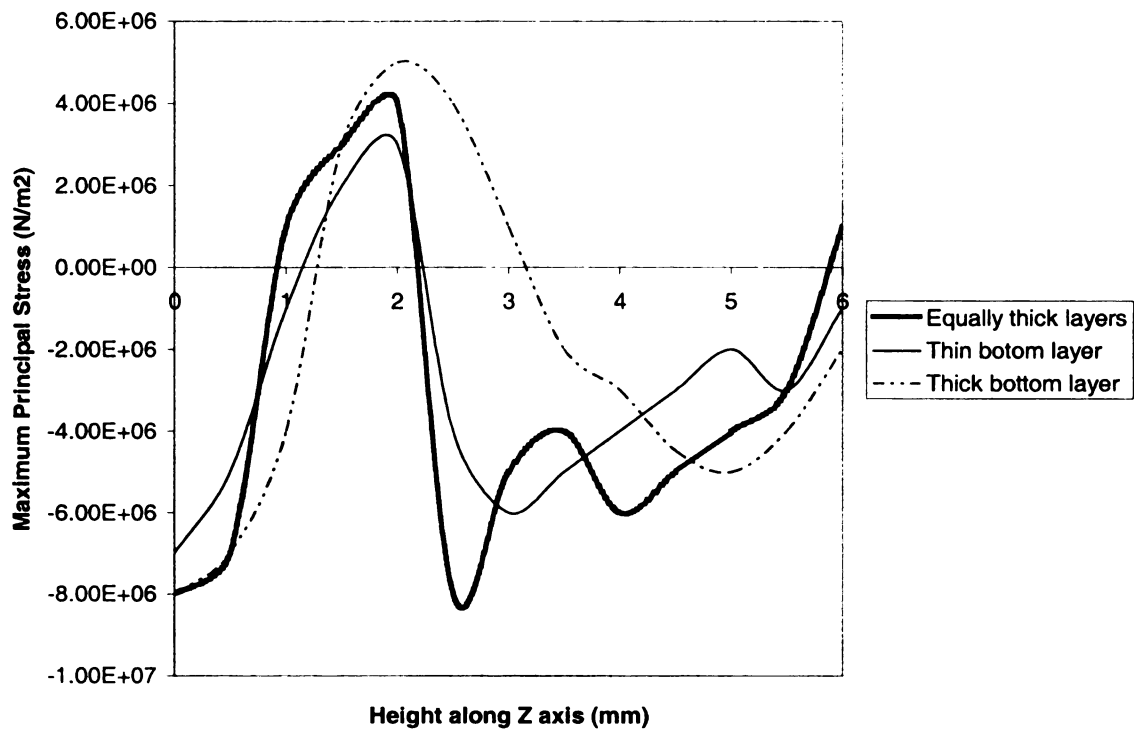
**Figure 28: Maximum principal stresses for the 3 layered FGM model
at x = 0, y = 0 mm**
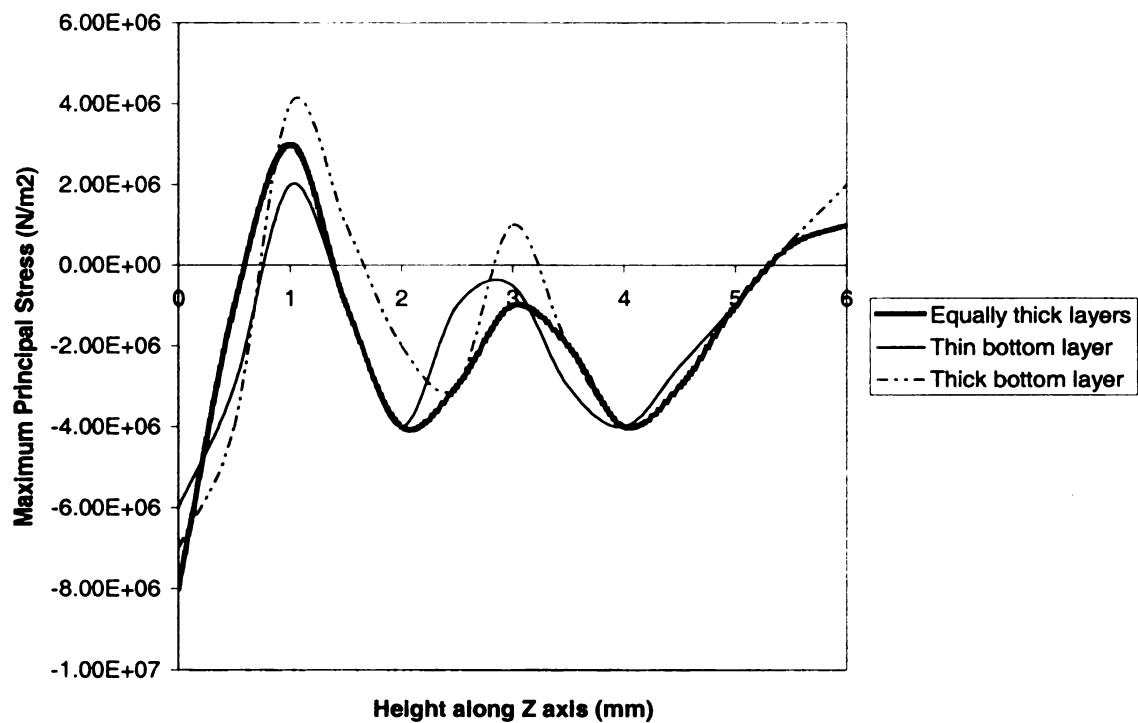
**Figure 29: Maximum principal stresses for the 6 layered FGM model
at x = 0, y = 0 mm**
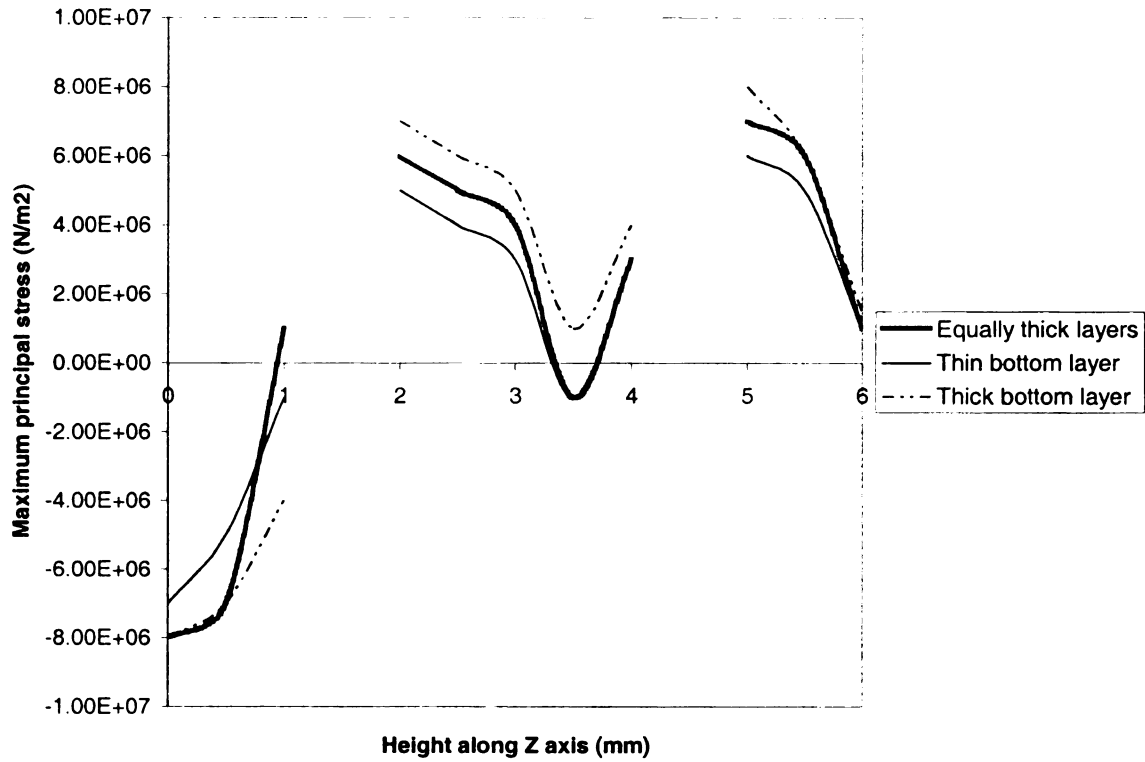
**Figure 30: Maximum principal stresses for the 3 layered FGM model
at x = 0, y = 3 mm**
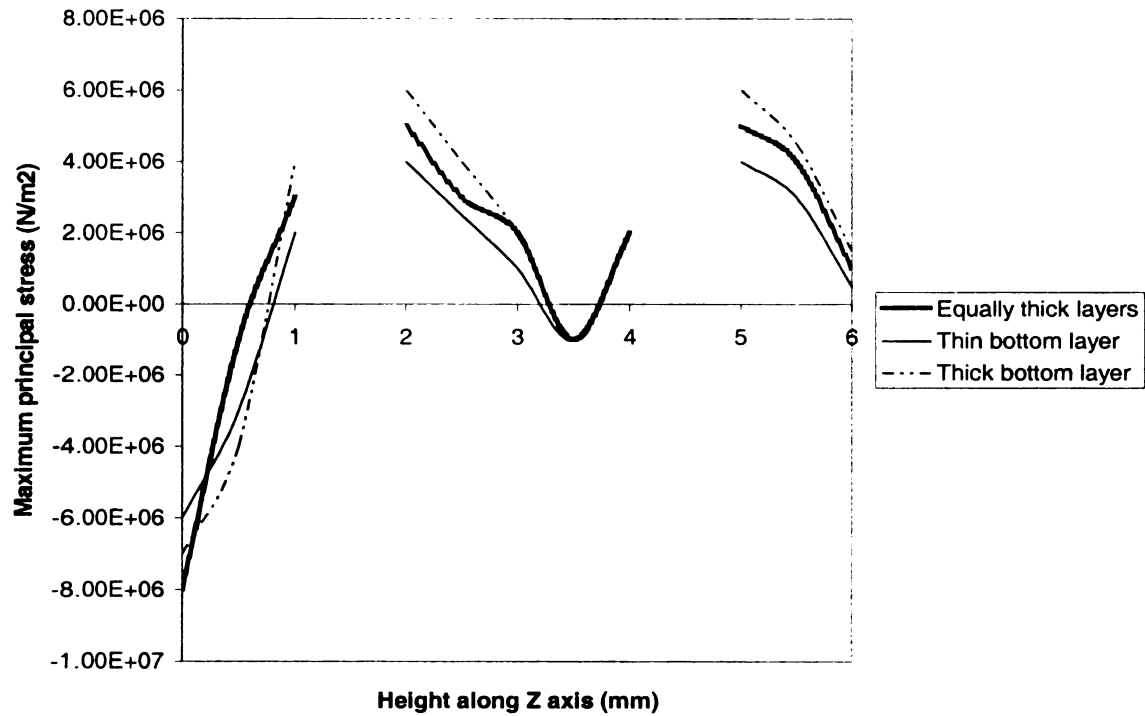
**Figure 31: Maximum principal stresses for the 6 layered FGM model
at x = 0, y = 3 mm**

Many studies in the past have looked at the effects of confining the brittle material [36]. In our case, the functionally gradient materials were modeled to fail at a tensile stress of 355 MPa which is also the tensile strength of alumina (lower of the two between zirconia and alumina). At this value of stress the material underwent brittle failure. Elastic perfect behavior was assumed for compressive behavior of the functionally gradient material and the Rankine failure criterion was used in the models. In all the cases, it was seen that the maximum principal stress in the models was well below the tensile limit.

For obtaining mesh convergence, the mesh was refined in all the areas until the required convergence limit was obtained. It was verified that the ratio of stress values between two successive refinements was less than 0.1%.

3.7 VALIDATION

For validating our results, the finite difference approach was used. A simplified case of a two dimensional two layered FGM model of alumina and PSZ zirconia with only one cooling channel was considered. Starting from the simplified momentum and energy differential equations for fully developed (velocity and temperature profiles) flow in the two-dimensional parallel wall channel, the convective heat transfer coefficient was calculated when there is a constant flux through the lower wall but the upper wall is insulated. The general steps that were followed are as follows:

i.   The laminar-flow solution to fully-developed channel flow was found and it was expressed in terms of the mean velocity V_m. For simplification, y=0 was chosen to be the mid-point of the channel.

From the continuity equation, we have:

$$\frac{\partial u}{\partial x} + \frac{\partial v}{\partial y} = 0$$

The X- momentum equation can be simplified to:

$$-\frac{1}{\rho}\frac{\partial P}{\partial x} + \nu\frac{\partial^2 u}{\partial y^2} = 0$$

And the Y-momentum equation to:

$$-\frac{1}{\rho}\frac{\partial P}{\partial y} = 0$$

On applying the boundary condition, u = 0 at y = ± h, and $\frac{\partial u}{\partial y} = 0$ at y = 0, we get:

$$u = -\frac{1}{2\mu}\frac{\partial P}{\partial x}(h^2 - y^2)$$

Now, the area weighted mean velocity is defined as,

$$V_m = \frac{\int_{-h}^{h} u\, dy}{\int_{-h}^{h} dy}$$

Solving the above equations we get,

$$u = \frac{3}{2}V_m(1 - \frac{y^2}{h^2})$$

ii.   The mixed-mean fluid temperature T_m for channel flow was defined and an overall energy balance (integrating over y the advection-diffusion equation) was calculated to relate q'' to dT_m/dx

53

Neglecting the term $\dfrac{\partial^2 T}{\partial x^2}$ for the long pipe and also the term $\mu\left(\dfrac{\partial u}{\partial y}\right)^2$ for low speed

flows, the thermal energy equation gives us:

$$\mu\frac{\partial T}{\partial x} = \alpha\frac{d^2 T}{\partial y^2}$$

Now let's define the mixed-mean fluid temperature T_m as,

$$T_m(x) = \frac{\displaystyle\int_{-h}^{h} uT\,dy}{\displaystyle\int_{-h}^{h} u\,dy}$$

On solving the above equations and applying the boundary condition q_{in} = constant on

the lower wall and $q_{out} = 0$ on the upper wall, we get:

$$\rho C_p V_m 2h\frac{\partial T_m}{\partial x} = q''_{in}$$

iii.   The dimensionless temperature profile is now defined as,

$$\theta = \frac{T_w - T}{T_w - T_m}\,,$$ where T_w is the wall temperature

For a fully developed temperature profile, by putting $\dfrac{\partial\theta}{\partial x} = 0$ and solving, we get:

$$\frac{\partial T_w}{\partial x} = \frac{\partial T}{\partial x}$$ and $$\frac{\partial T_w}{\partial x} = \frac{\partial T_m}{\partial x}$$

iv.   By using all of the above results, and on integrating the advection diffusion

equation twice we can find T(y). Then using the definition of T_m and substituting

the above result, we get:

$$T_m = T_w - \frac{V_m}{\alpha}\frac{dT_m}{dx}h^2\left(\frac{52}{35}\right)$$

v. Combining all the results and using $q'' = H(T_w - T_m)$, where H is the convective heat transfer coefficient, we get:

$$H = \frac{35k}{26h}$$

In our case, we consider a channel with cross-section of 4mm X 2mm. Further, for the sake of simplicity in calculations we consider our block to be 16mm X 16mm X 6mm in dimension, and simplify it further to a 2D model with 16mm X 6mm dimensions. Adopting a grid space of $\Delta x = \Delta y = 1$ and identifying the line of symmetry, the foregoing nodal network is constructed. The corresponding finite-difference equations may be obtained by applying the energy balance method to nodes 1 to 61.
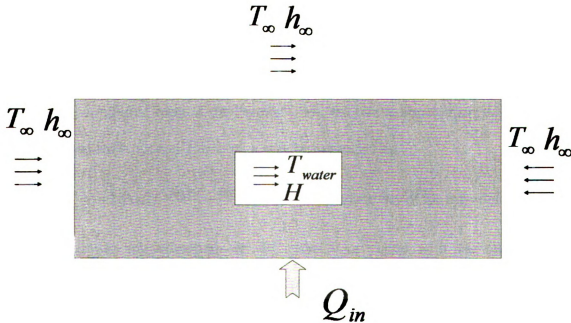
Figure 32: The two dimensional model for validation
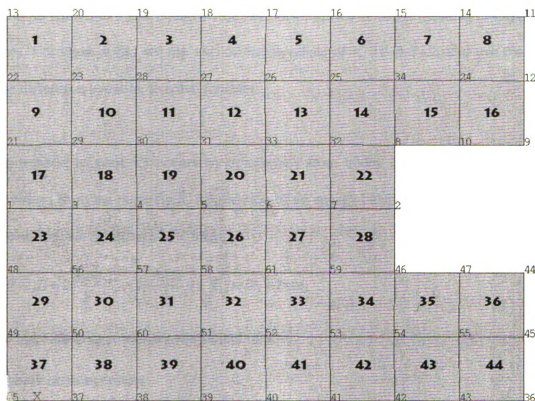
Figure 33: Meshing the symmetric model for finite-difference calculations

For all interior nodes, net heat flux flowing in is equal to zero. Referring figure 33,

$$\sum_{i=0}^{4} q_{(i)\longrightarrow(m,n)} = 0$$

So by using simplified form of the Fourier's law, the rate at which energy is transferred by conduction from node m-1, n to m, n may be expressed as,

$$q_{(m-1,n)\longrightarrow(m,n)} = k(\Delta y.1)\frac{T_{m-1,n} - T_{m,n}}{\Delta x}$$, where k = conductivity of the material

Applying similar approximations on all nodes in a region with the same material properties, we obtain the following equation for all those interior nodes:

$$T_{m,n+1} + T_{m,n-1} + T_{m+1,n} + T_{m-1,n} - 4T_{m,n} = 0$$

For nodes from 1 to 7, the equations cannot be simplified as above because of different k values. For these nodes we use two different values of k, k1 and k2, and use the basic finite difference equation to solve for them.

Heat transfer to node 13 occurs by conduction from nodes 20 and 22, as well as by convection from the outer fluid. Application of an energy balance to this section yields a finite-difference equation of the form,

$$(T_{20} + T_{22}) + 2\frac{h_0\Delta x}{k}T_\infty - 2\left(\frac{h_0\Delta x}{k} + 1\right)T_{13} = 0 \text{, where,}$$

h_0 = convective heat transfer coefficient of air

T_∞ = bulk air temperature

k = conductivity of the material – either k1 or k2

Nodes 14 to 20, 1, 21, 22, 48 and 49 have the same physics (3 conduction, 1 convection) and application of an energy balance to node 14, as an example, yields a finite-difference equation of the form:

$$T_{11} + T_{15} + 2T_{24} - 2\left(\frac{h_0\Delta x}{k} + 2\right)T_{14} = -\frac{2h_0\Delta x}{k}T_{\infty,0}$$

For nodes 2, 10 and 47 h_0 is replaced with H of water, and T_∞ with T_{water}.

For nodes 12 and 45 (3 conduction, 1 adiabatic), taking node 12 as an example, it follows that,

$$T_9 + 2T_{24} + T_{11} - 4T_{12} = 0$$

57

Nodes 8 and 46 are internal corners for which, taking node 8 as example,

$$2T_{32} + 2T_{34} + T_2 + T_{10} - 2\left(3 + \frac{H\Delta x}{k}\right)T_8 = -2\frac{H\Delta x}{k}T_{water}$$

On the bottom line, a heat flux Q is applied. So, each element will have a heat flux of Q/8. So, nodes 37 to 43 have a heat flux of Q/8 and nodes 35 and 36 have a heat flux of Q/16. Again using the principle of heat balance on these nodes we get,

$$\sum_{i=0}^{4} q_{(i)\longrightarrow(m,n)} = 0$$

Applying the above relations we can solve for nodes 35 to 43.

In case of nodes 9 and 44, heat transfer is characterized by conduction from two adjoining nodes and convection from the internal flow, with no heat transfer occurring from an adjoining adiabat. Performing an energy balance for nodal region 18, it follows that:

$$(T_{12} + T_{17}) - \left(\frac{H\ \Delta x}{k} + 2\right)T_{18} = -\frac{H\Delta x}{k}T_{water}$$

For node 11, H of water is replaced with h_0, and T_{water} with T_∞.

For validation purpose a low value of heat flux, 10,000 W/m², was used to minimize the error due to a coarse mesh. Also, from the relation,

$$H = \frac{35k}{26h},$$ by plugging in the value of h = 1mm and k_{water} = 0.6 W/m/K,

we get H = 807.7 W/m²/K.

Using $h_\infty = 15$ W/m²/K, and $T_\infty = 25°C$, we solve the above finite-difference equations. The nodal temperatures obtained from the above calculations are tabulated in Table 3. These results are then compared with those obtained from a finite element model solved in *Ansys 7.0*. The FE model used is a 3-D cylinder with radius of 8 mm and a thickness of 6mm. An inlet velocity of 0.3 m/s (Re = 800) and inlet temperature of 25°C for water was used with outlet pressure set to atmospheric. Convection was modeled all external surfaces except the bottom surface where a heat flux of 10,000 W/m² was applied.
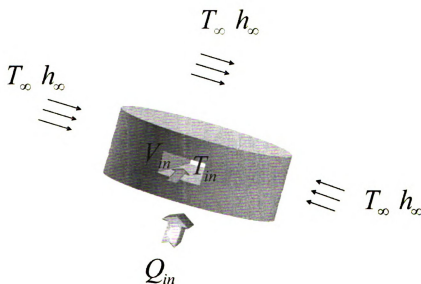
Figure 34: Finite element model with one cooling channel, used to compare results obtained from the finite difference calculations

It can be seen that considering the very rough estimate of the model, the nodal temperatures are within reasonable comparable limits. The Ansys finite element model was also solved for thermal strains by using a 2D coupled element. The results were then compared with the hand calculated results.

For hand calculation of stress along the X axis, first the temperature was averaged in the area with material 1, from elements 1 to 22, and the steady state averaged temperature denoted by T_1. Then similarly the temperature was averaged in the area with material 2, from elements 23 to 44, and denoted by T_2. The materials would tend to elongate along the X axis, and their final elongated lengths if allowed to expand can be defined as:

$L_i = l(1 + \alpha_i(T_i - 25))$, where:

α_i = Coefficient of thermal expansion of the materials

l = Initial length = 16 mm, and,

T_i = Final steady state averaged temperature of the materials

Depending on the value of α, one material would tend to expand more than the other. Now, this is assumed to be similar to a bimetallic strip, and the final elongated length of both areas is assumed to be L_m. To achieve equilibrium, the compressive force exerted by one area should equal the tensile force of the other. So, in other words considering the 2D layers to be also l mm wide (normal to the paper), we have:

$\sigma_1 t_1 l = \sigma_2 t_2 l$, where $t_1 = t_2$ = respective layer thicknesses = 3 mm

or $\sigma_1 = \sigma_2$ and $E_1 \varepsilon_1 = E_2 \varepsilon_2$, where

E_1 and E_2 are the respective Young's modulus, and,

ε_1 and ε_2 are the respective strains

Now, $\varepsilon_i = \dfrac{L_m - L_i}{L_i}$, where subscript i denotes either layer 1 or layer 2.

Hence, on solving the above equations, we get:

$$L_m = \frac{L_1 L_2 (E_1 + E_2)}{(E_1 L_2 + E_2 L_1)}$$

Table 3: Comparing nodal temperatures from the hand calculated FD model with the Ansys FE model

T_{FD} (°C) = Nodal temperature hand calculated using the finite difference scheme

T_{FE} (°C) = Nodal temperature obtained from the *Ansys* finite element model

Node	T_{FD} (°C)	T_{FE} (°C)	Node	T_{FD} (°C)	T_{FE} (°C)	Node	T_{FD} (°C)	T_{FE} (°C)	Node	T_{FD} (°C)	T_{FE} (°C)
1	45.3	34.7	17	41.5	33.7	33	42.9	33.1	49	45.2	34.6
2	41.7	33.9	18	42.6	32.5	34	39.1	29.6	50	45.1	34.4
3	45.2	34.7	19	43.1	32.8	35	45.7	34.7	51	44.9	34.1
4	44.9	34.5	20	43.4	33.3	36	44.1	34.3	52	44.8	33.9
5	44.5	33.9	21	44.2	33.7	37	45.4	34.7	53	44.4	33.7
6	44.1	33.6	22	43.8	33.7	38	45.2	34.6	54	44.3	33.5
7	43.6	32.6	23	43.6	33.6	39	45.1	34.4	55	44.1	33.4
8	37.4	27.7	24	36.5	27.6	40	44.8	34.3	56	45.1	34.4
9	34.7	26.0	25	40.2	32.4	41	44.6	34.2	57	45.0	34.4
10	35.2	26.8	26	41.5	33.7	42	44.3	34.1	58	44.7	34.4
11	36.1	27.4	27	41.9	34.1	43	44.2	34.1	59	44.2	34.0
12	36.0	27.3	28	42.7	33.0	44	42.9	32.8	60	45.1	34.4
13	43.8	32.7	29	44.2	33.7	45	43.8	33.1	61	44.3	33.5
14	37.4	27.7	30	43.8	33.7	46	42.6	32.6			
15	38.2	29.4	31	43.5	33.5	47	42.1	32.4			
16	40.2	32.4	32	41.3	32.8	48	45.4	34.7			

Now, say layer 2 tends to expand more than layer 1 along the X axis. So compressive stress in layer 2 would be:

$$\sigma_2 = -E_2 \left(\frac{L_2 - L_m}{L_2} \right), \text{ where } L_2 > L_m > L_1$$

And tensile stress in area 2 would be:

$$\sigma_1 = +E_1 \left(\frac{L_m - L_1}{L_1} \right)$$

Plugging in the value, the tensile stress in layer 1 (bottom layer) was found to be 1.87 E6, and the compressive stress in layer 2 (top layer) was found to be − 1.87 E6. The average tensile stress in layer 1 from the FE Ansys model was found to be 2.57 E6, and the average compressive stress in layer 2 was - 2.87 E6. It was thus seen, that considering the very rough estimate of the model, the elemental stresses were within reasonable comparable limits when compared with the finite element model.

3.8 CONCLUSIONS

The idea of using 8 cooling channels was useful as it could bring down the temperature in the operating range of the device. It was observed that the high thermal gradient created by the cooling channels results in high induced thermal stresses in the specimen. Hence to offset this effect the concept of using a material with functionally gradient properties was used.

From the results of the analysis, it can be inferred that the stresses in the FGM models were considerably less than the stresses in the alumina model. Hence it can be said that

the idea of using the FGM can be justified. The stresses in the six layered FGM model were further found to be lower than those in the three layered FGM model. Varying the thickness of the layers of the FGM also revealed interesting results. For both cases of a three layered and a six layered model, it was found that the model with a thinner bottom layer had a lower value of stress than the other combinations.

3.9 RECOMMENDATIONS FOR FUTURE WORK

As far as future work on this topic is concerned, currently attempt is being made to powder process a three layered FGM model. Work can be done on finding what should be the optimum ratios of layer thicknesses. Experimental validation of the heat exchanger should of course be the final goal. Graphite can be used as the fugitive phase for making the internal channels and the heat exchanger can then be tested under actual conditions.

4. COMPUTATIONAL STUDY OF MIXING MICROCHANNEL FLOWS

Ever-improving technological advances in micro and nano fabrication have encouraged renewed interest in mixing through topological or chaotic flows. Particular attention has been paid to geometries that are sufficiently small because neither turbulent (owing to the low Reynolds number), nor active (owing to the difficulty in micromachining moveable or easily controlled parts) mechanisms are feasible. Examples of recent successful strategies include a "staggered herringbone" micromixer [37] in which two species were mixed well beyond the diffusion limit simply through patterning the bottom of a channel 200 microns in width.

Motivated by recent experimental advances [37, 38] in microfluidic mixers, we study the passive mixing and flow properties of a ribbed micro-channel by means of computational fluid dynamics (CFD). Such geometries overcome the low Reynolds number boundaries to efficient mixing by creating a three dimensional flow that yields chaotic trajectories. It is hoped that such CFD studies advance both the capabilities and the understanding of such micro-patterned mixing flows. After studying several properties of the flow which are not experimentally accessible, we studied mixing in: (i) channel with two pairs of inclined ribs (ii) identical channel with no ribs. We also study the pressure drop along the length of the channel, which limits the velocity and therefore the time necessary for effective mixing. Advantages of full CFD studies of micromixing include the ability to visualize species densities at any point in the volume without optical challenges of confocal-microscopy.

4.1 CHANNEL DESIGN AND SPECIFICATIONS

To study the differences in mixing rates two geometries of microchannels, one of them as shown in figure 10, were built. All the channels are square in cross-section with sides of 1.6 mm and are all 20 mm long. The straight ribless channel only allows one-dimensional flow of the fluid. On the other hand, the ribbed channel has a 3-dimensional geometry with two pairs of inclined ribs. Near the inlet the ribs were on the top and bottom sides of the duct, while near the outlet the inclined ribs were placed on the two opposite side walls. Each ribbed pair consists of ten ribs in each straight duct, five on the leading wall and five on the trailing wall, all with the same pitch. The ribs on those two walls are staggered relative to each other with he ribs on the leading wall offset from those on the trailing wall by a half pitch. All ribs are inclined with respect to the flow at an angle of 45 degrees. The cross-section of the rounded ribs is made up of three circular arcs of radius R, where R equals 0.08 mm so that the rib height is 0.16 mm and the rib-height to hydraulic-diameter is 0.1. The pitch to height ratio is 5.

4.2 MESH GENERATION

When computing ducts with ribs, it is important for the geometry of the ribs to be captured correctly. This is because they exert considerable influence on the flow and heat transfer. Shih, et al [30] studied the effect of a ribbed U-duct with or without rotation. Their model consisted of a U-duct with inclined ribs on just two opposite faced walls. They developed a mesh capturing the effects of the side ribs to perform computational fluid dynamics simulations.

We used the code written by Shih et al [30], which was modified to represent our geometry. The code by Shih et al [30], which was in NASA plot3D format, was first converted to ASCII dat format readable by Gambit a CFD meshing tool. Then a code in C++ was written [Appendix A] to cut the grid and modify it according to the required geometry. Later, the modified grid was imported into Gambit where the boundary conditions were applied.

The domains of the smooth and ribbed ducts were replaced by H-H structured grids (Figure 35). The number of grid points in the streamwise direction from inlet to outlet was 255 for the smooth duct and 761 for the ribbed duct. Whether smooth or ribbed, the number of grid points in the cross-stream plane was 65 X 65. The number of grid points and their distribution were obtained by satisfying a set of rules such as aligning the grid with the flow direction as much as possible, keeping the grid aspect ratio near unity in regions with recirculating flow.

4.2 MODELLING DETAILS, INITIAL AND BOUNDARY CONITIONS

After modifying the mesh using our C++ code, the model was imported into Gambit V. Using Fluent 6.0 specific boundary conditions, channel walls were defined, the two inlets were defined as "velocity inlets" and the outlet was defined as "outflow". The volume of the channel was defined as "fluid. The meshed models are shown in Figure 35.

The models were then checked and exported to Fluent 6.0 for performing flow and mixing computations. The Multiphase Solver in Fluent was used to solve for mixing of two fluids entering the microchannel. Initially two liquids with identical properties as

that of water were used to analyze mixing. Later, the mixing simulations were run for a variety of combinations of different liquids. The properties of the liquids used are listed in Table 4. A segregated steady-state solver with Mixture Multiphase model was used. Standard operating conditions of pressure were specified.
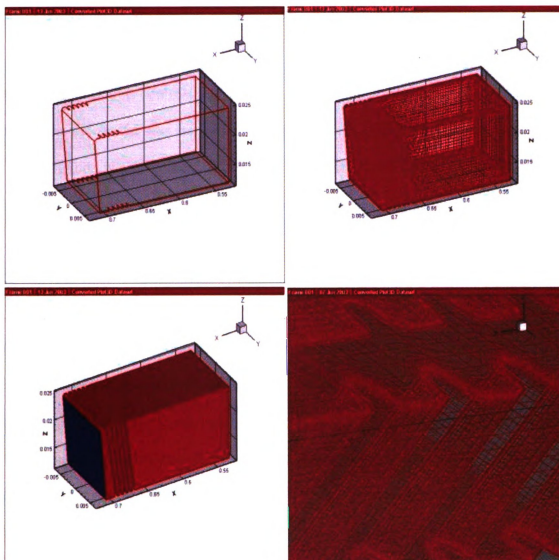
Figure 35: Meshing of ribbed-duct

At inlet 1, a volume fraction of 1 was specified for liquid 1 and a volume fraction of 0 was specified for liquid 2. Similarly, at inlet 2, a volume fraction of 1 was specified for

liquid 2 and 0 for liquid 1. Equal velocity magnitudes ranging from 0.1 m/s to 1.5 m/s were specified to investigate mixing. For the channel height and width specified, and the hydraulic diameter calculated as 1.6 mm, the velocities correspond to Reynolds numbers from 10 to 1500 depending on fluids used. The outlet of the channel was given a zero-boundary condition for all flow variables.

Appropriate solution controls and residual monitors were set. After setting zero initial conditions the model was iterated. Depending on the velocity magnitudes, about 600-1500 iterations were required to achieve convergence. The end of the simulation was verified by a quick check to see that the flow field for the entire channel was solved.

4.3 SIMULATION RESULTS

4.3.1 FLOW PATTERN

Velocity vectors and coordinate positions were plotted in Fluent to obtain vector plots. To obtain the plot, a horizontal center plane was defined for the ribbed and ribless ducts, and the top view of the plane was plotted in Fluent. These plots were used to check for the formation of secondary flow and flow separation for an indirect verification of chaotic advection. Figure 36, shows the velocity vectors plotted on the center plane along the length of the ribbed duct for a water-water mixing at Re = 800. Figure 36, in this thesis is presented in color.
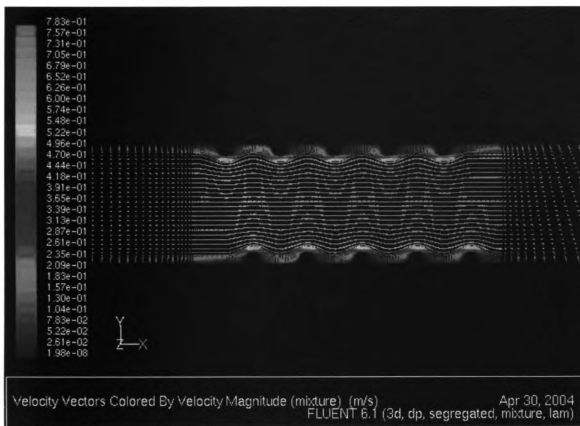
Figure 36: Velocity vectors of the ribbed duct for water-water mixing at Re = 800

A high speed core velocity is formed in the ribbed ducts with the highest velocities were in the ribbed region. The chaotic high speed flow in the ribbed region indicates mixing of the two fluids.

4.3.2 MIXING

For investigating mixing along the channels, contour plots of concentration or volume fraction of liquid 2 were plotted in Fluent. The blue color at inlet1 indicates a volume fraction of 0 and red color at inlet 2 indicates a volume faction of 0 for liquid 2. Green indicates a volume fraction of 0.5 which is the desired result for perfect mixing. The plots show how the volume fraction approaches 0.5 as the two liquids mix as they flow along

the length of the channel. For the case of water-water mixing, it can be seen that the two fluids mix almost completely in the first set of ribs (a) in the ribbed duct. In the ribless duct (b), the fluids hardly mix at all outside of their interfacial area along the center of the channel. The water-glycerin mixture takes considerable longer time to mix and they are nearly mixed only at the end of the second set of ribs. Figures 37 to 42 show the volume fraction contours of one of the mixing fluids. These contour plots in this thesis are presented in color. A more detailed analysis of these simulation results and differences is provided in the next section.
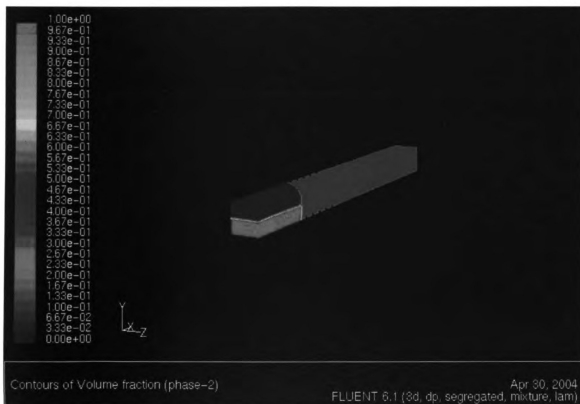
Figure 37: Contour plots of volume fraction of liquid 2 in water-water mixing in the ribbed duct with inlet velocity = 0.5m/s (isometric view)
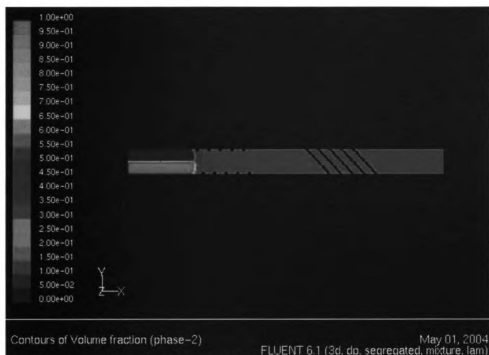
Figure 38: Contour plots of volume fraction of liquid 2 in water-water mixing in the ribbed duct with inlet velocity = 0.5m/s (cross-sectional view)
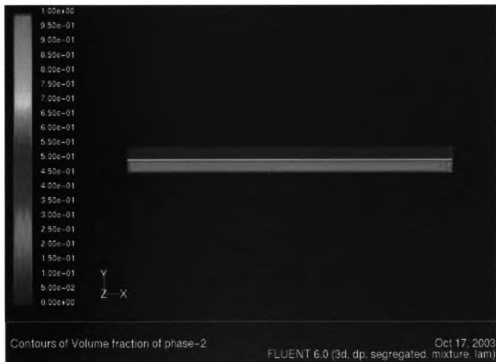
Figure 39: Contour plots of volume fraction of liquid 2 in water-water mixing in a ribless duct with inlet velocity = 0.5m/s (cross-sectional view)
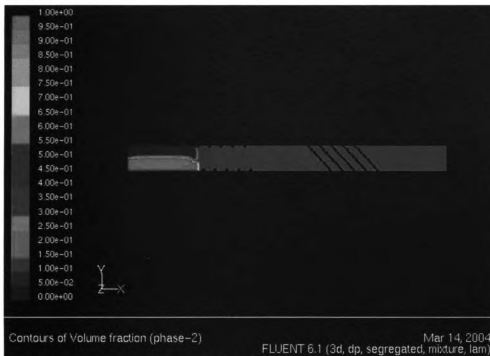
Figure 40: Contour plots of volume fraction of liquid 100 times more viscous than water when mixed with water in a ribbed duct with inlet velocity = 0.5m/s (cross-sectional view)
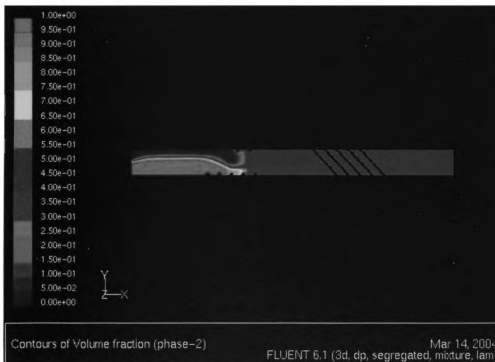
Figure 41: Contour plots of volume fraction of liquid 300 times more viscous than water when mixed with water in a ribbed duct with inlet velocity = 0.5m/s (cross-sectional view)
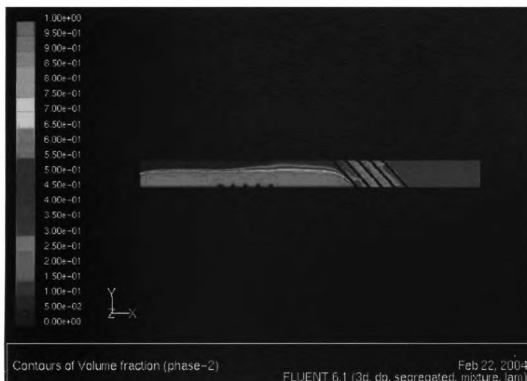
Figure 42: Contour plots of volume fraction of water-glycerin mixing in a ribbed duct with inlet velocity = 0.5m/s (top view)

4.4 ANALYSIS OF RESULTS

To better characterize mixing in these channels and to provide a quantitative treatment of analysis, "cross-sections" were defined for all the models. Four cross-sections were defined – one each before and after each set of ribs, to observe how mixing occurs along the entire depth of the duct and to see if recirculation in the plane perpendicular to the direction of flow occurs.

4.4.1 CHARACTERIZING MIXING

Mixing characteristics were analyzed in the cross-sections and simulations were run in each of the two types of ducts for different inlet velocities and different combinations of

fluid mixtures. For each run, volume fraction plots were obtained and the data values of volume fraction of liquid2 calculated in the zone of nodes included in the cross-sections were exported to MATLAB to obtain statistics. The summary of all runs is tabulated in Tables 4 and 5. In Tables 4 and 5, the first three columns tabulate the inlet velocities and the corresponding Re values. The average values of volume fraction of liquid2 calculated for the four cross-sections are tabulated. Clearly average values were found to be poor indicators of mixing as can be seen for the case of the ribless duct where the values are 0.5. 'Mixing' here takes place only at the interface of the two liquids and the volume fractions remain fairly constant along the duct at regions further apart from the interface.

4.4.2 MIXING RATES AND EFFICIENCIES

Since we are trying to characterize the mixing rate by the values of the volume fraction which is a conserved quantity, as the volume fraction of a fully mixed fluid is 0.5, the standard deviation in composition was considered to be an approximate estimate for mixing. This was actually confirmed by literature by Baker et al [29], who noted that the most widely used measure of composition uniformity is the Coefficient of Variation, (CoV), which is the ratio of the standard deviation in composition, (RMSD) and the mean composition (AVG). These statistics are defined below:

$$AVG = \frac{\sum X_i}{N} \; ; \text{Mean}$$

$$DEVSQ = \sum \left(X_i - \bar{X}_i \right)^2 \; ; \text{Square of deviations}$$

$$RMSD = \sqrt{\frac{DEVSQ}{N-1}} \; ; \text{Root Mean Square Deviation } (\sigma)$$

$$\text{CoV} = \frac{RMSD}{AVG} \text{; Coefficient of Variation}$$

Here X_i represents the value of volume fraction of liquid2 calculated for the ith node in the sample and N represents the total number of data points present in the sample of the cross-section. CoV of 1% or less (<0.01) was given as a general rule of thumb in the literature for blending of colors to uniformity. A CoV of 1%, in other words, indicates 99% complete mixing.

Using this definition for mixing rate, values of CoV were calculated in MATLAB [Appendix B] for each of the runs. The values are tabulated in Table 4 for a few cases.

It is seen that in the case of ribbed ducts, the CoV drops rapidly from 5% at the lowest Reynold's number to less than 1% at Re > 50. The CoV in fact drops to less than 0.1% at Re > 100. This indicates an extremely efficient mixing.

In the ribless ducts, the CoV is constant around 0.8. Although no mixing is expected to take place, the CoV is not 1 because of the limited mixing at the interface of the liquids as they move along the straight channel. Thus mixing is only about 20% complete in the ribless duct, an extremely poor rate when compared to the ribbed ducts.

Table 4: Simulation results tabulated for the ribbed duct

Density of water	1000 kg/m³	Channel Height	1.6 mm
Kinematic viscosity of water	0.001kg/ms	Channel Width	1.6 mm
Density of liquid A	1000 kg/m³	Hydraulic Diameter	1.6 mm
Kinematic viscosity of liquid A	0.01kg/ms	Re_w= Reynolds No. of water	
Density of liquid B	1000 kg/m³	c = Cross-Section	
Kinematic viscosity of liquid B	0.03kg/ms	vf2 = Volume fraction of liquid 2	
Density of glycerin	1259.9 kg/m³		
Kinematic viscosity of glycerin	0.799kg/ms		

		Average of vf2				Statistics for c 4		
Mixtures	Avg Re_w	c1	c2	c3	c4	DEVSQ	RMSD	CoV
Water-Water	400	0.604	0.5	0.5	0.5	2.4E-05	3.9E-04	7.9E-04
Water-Water	800	0.592	0.5	0.5	0.5	5.2E-06	1.8E-04	3.6E-04
Water- Liquid A	400	0.437	0.5	0.5	0.5	0.0043	0.0052	1E-02
Water- Liquid A	800	0.467	0.5	0.5	0.5	4.8E-05	5.5E-04	1.1E-03
Water- Liquid B	400	0.615	0.443	0.51	0.5	0.1346	0.0291	5.8E-02
Water-Liquid B	800	0.608	0.466	0.51	0.5	0.0417	0.0162	3.2E-02
Water-Glycerin	400	0.746	0.674	0.64	0.5	0.206	0.036	7.2E-02
Water-Glycerin	800	0.738	0.65	0.61	0.5	0.0358	0.015	2.9E-02

Table 5: Simulation results tabulated for the ribless duct

Mixtures	Avg Re_w	Average of vf2				Statistics for c 4		
		c 1	c2	c3	c4	DEVSQ	RMSD	CoV
Water-Water	400	0.5	0.5	0.5	0.5	26.079	0.4050	8.1E-01
Water-Water	800	0.5	0.5	0.5	0.5	26.079	0.4050	8.1 E-01
Water- Liquid A	400	0.54	0.52	0.52	0.52	31.798	0.4472	8.6E-01
Water- Liquid A	800	0.53	0.52	0.52	0.52	31.798	0.4472	8.6E-01
Water- Liquid B	400	0.58	0.56	0.55	0.55	36.405	0.4785	8.7E-01
Water-Liquid B	800	0.57	0.56	0.55	0.55	37.2467	0.484	8.8E-01
Water-Glycerin	400	0.57	0.56	0.55	0.55	42.298	0.5170	9.4E-01
Water-Glycerin	800	0.55	0.55	0.54	0.54	41.4045	0.5103	9.45E-01

4.5 RESULTS AND DISCUSSION

4.5.1 Effectiveness of Microchannel System

The above analysis reveals some interesting results. The value of CoV calculated at a cross-section indicates the amount of mixing that has taken place between the two fluids when they pass through the cross-section. In case of the ribbed duct the mixing rates were found to be much higher than the ribless duct. Taking the ratios of CoV calculated at cross-section 4 for the two ducts for Re of water = 800, the results indicate that the ribbd duct produced about 100 times more mixing than the ribless duct.

We expect mixing in the ribless duct to decrease rapidly with increasing Reynolds number due to corresponding decrease in residence times. Thus it has an inverse relationship with diffusion-dominated mixing and Reynolds number [28]. However, since diffusion is not modeled here, the mixing rate is expected to be independent of Reynolds number. The results obtained in the simulation strongly correlates with this expectation. The CoV values obtained for the case of water-water mixing are constant at 0.8 for all Reynolds numbers.

4.5.2. Validation of results

Although the models have not been directly validated with any experimental or theoretical results, their correlation of the general trends in mixing and with those of Liu et al [28] builds confidence in the simulation models. Since the criteria for design of the micromixers were defined in terms of the occurrence of chaotic advection, it was decided to look at the conditions and indicators of chaotic mixing in simulation models as the next step in validation.

The flows around the ribs should be three-dimensional with secondary flows being generated in the channel cross-section in addition to the bulk flow along the axis of the channel. The secondary flows in combination with the axial flow distort and stretch material interfaces and can produce chaotic advection which leads to rapid mixing (Liu et al, [28]). Thus secondary flows are expected to occur in the ribbed duct. The ribless duct only allows one dimensional flow o the fluid and hence no chaotic advection is expected to occur.
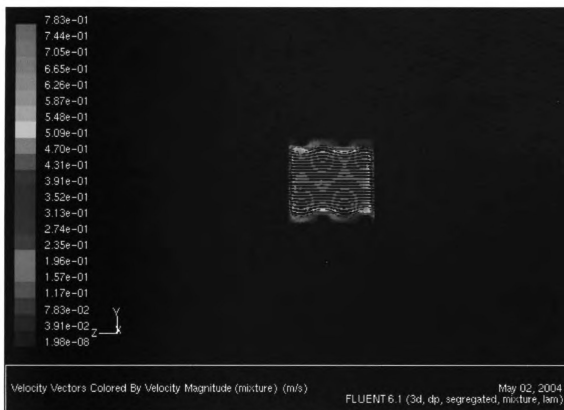
Figure 43: Velocity vectors in a cross-section in the ribbed area

Secondary flows occur in the ribbed duct because the ribs stir and rotate the fluid. This was confirmed by the plot of velocity vectors at a rib cross-section (Figure 43). The figure in this thesis is presented in color. It was concluded that the rapid mixing and strong secondary flow is consistent with the occurrence of chaotic advection.

4.6 FABRICATION OF MICROCHANNELS

The same technique was used to manufacture the ribbed internal channels as described earlier (Chapter 3). Graphite was used as the fugitive phase in the shape of desired channels during compaction, which decomposes during sintering leaving cooling, channels (Figures 7 and 8). Ribs were machined onto the graphite pieces using CNC

controlled machines. The idea of using a fugitive phase was really advantageous as we could machine out the complicated rib geometry with ease using a CNC controlled machine. Hence, we were able to successfully process internal channels of the given geometry.

4.7 FUTURE WORK

Immediate work is proposed to validate the results of the CFD analysis by performing a series of detailed experiments on the ribbed ducts. An arrangement could be set up such that we have water flowing into the channel through Inlet 1 and blue ink through Inlet 2. The experiments can then be used to track particles and image along various depths of the channel, and the results compared with the ribless ducts.

4.8 CONCLUSIONS AND EXTENSIONS

While CFD is clearly useful for illuminating the details of chaotic mixing flows, a more exciting application would be optimization. In particular, a systematic study over many parameter values (groove depth, width, spacing, Reynolds number, etc...) could be of great benefit both to those interested in building better mixers and those interested in understanding how and why they work. An even more appealing numerical study would be an automated iterative parametric optimization, using Fluent as a "black box" to calculate and return mixing length (or any other appropriate mixing metric) to an optimization routine suited for multidimensional parameter space searching, e.g., a Nelder-Mead simplex method. One may also try other experimentally plausible geometries, limited only by the capabilities of current micro-machining and powder processing techniques.

APPENDIX A

C++ code to modify the CFD grid that was borrowed from Dr. T. Shih

```
#include <fstream>

#include <cassert>

#include <iostream>

#include <stdio.h>

#include <stdlib.h>

#include <unistd.h>

#include <string>

#include <iomanip>

#include <vector>

using namespace std;

void findminmax(vector<double> vectorarray, double &min, double &max)

{

  for(int p = 0; p < vectorarray.size(); p++)

  {

    if (p == 0)

    {

      min = vectorarray[p];

      max = vectorarray[p];

    }
```

```
else

    {

      if( min > vectorarray[p])

       min = vectorarray[p];

             if( max < vectorarray[p])

      {

      max = vectorarray[p];

             }

      }

    }

}


int main()

{

  double i,j,k,m;

  vector<double> ivalue;

  vector<double> jvalue;

  vector<double> kvalue;

  vector<double> mvalue;

  double ivaluemin,ivaluemax,jvaluemin,jvaluemax,kvaluemin,kvaluemax;

  double precisioni, precisionj, precisionk;

  string inputFilenameB;
```

```cpp
string comments1, comments2, comments3, comments4, comments5, comments6,
comments7, comments8;

cout << "please enter the input file name: ";

getline(cin, inputFilenameB);        // reading line

ifstream instreamB;

instreamB.open(inputFilenameB.data());

assert(instreamB.is_open());


getline(instreamB,comments1);        // reading line

getline(instreamB,comments2);

getline(instreamB,comments3);

getline(instreamB,comments4);

getline(instreamB,comments5);

getline(instreamB,comments6);

getline(instreamB,comments7);

getline(instreamB,comments8);


string Imatch = "I=";

string Jmatch = "J=";

string Kmatch = "K=";

string comm = ",";

string::size_type pos1 = comments7.find (Imatch,0);

string::size_type pos11 = comments7.find (comm,pos1);
```

```cpp
string::size_type pos2 = comments7.find (Jmatch,0);

string::size_type pos21 = comments7.find (comm,pos2);

string::size_type pos3 = comments7.find (Kmatch,0);

string::size_type pos31 = comments7.find (comm,pos3);

string Inumber = comments7.substr(pos1+2,pos11-pos1-2);

string Jnumber = comments7.substr(pos2+2,pos21-pos2-2);

string Knumber = comments7.substr(pos3+2,pos31-pos3-2);


int Ivalue = atoi(Inumber.c_str());

int Jvalue = atoi(Jnumber.c_str());

int Kvalue = atoi(Knumber.c_str());


cout << "Ivalue is " << Inumber << "   Jvalue is " << Jnumber << " Kvalue is " <<
Knumber << endl;


cout << " Total Number is " << Ivalue * Jvalue * Kvalue << endl;

for( int p = 0; p < Ivalue * Jvalue * Kvalue ; p++)

    {

    instreamB >> i;

    ivalue.push_back(i);

    }


for( int p = 0; p < Ivalue * Jvalue * Kvalue ; p++)
```

```cpp
{

instreamB >> j;

jvalue.push_back(j);

}

for( int p = 0; p < Ivalue * Jvalue * Kvalue ; p++)

{

instreamB >> k;

kvalue.push_back(k);

}

for( int p = 0; p < Ivalue * Jvalue * Kvalue ; p++)

{

instreamB >> m;

mvalue.push_back(m);

}


findminmax(ivalue,ivaluemin,ivaluemax);

findminmax(jvalue,jvaluemin,jvaluemax);

findminmax(kvalue,kvaluemin,kvaluemax);

cout << " i value Min and Max = " << setprecision(10) << ivaluemin << "   " <<
ivaluemax ;

cout << " j value Min and Max = " << setprecision(10) << jvaluemin << "   " <<
jvaluemax ;
```

```cpp
cout << " k value Min and Max = " <<  setprecision(10) << kvaluemin << "   " <<

kvaluemax ;

instreamB.close();

// printing output file

//fflush(cin);

cout << "Enter the name of the Output File: ";

string outputFile;

getline(cin,outputFile);

ofstream outStream(outputFile.data());

assert(outStream.is_open());


cout << "please enter the Magnification Factor for X: ";

cin >> precisioni;

cout << "please enter the Magnification Factor for Y: ";

cin >> precisionj;

cout << "please enter the Magnification Factor for Z: ";

cin >> precisionk;


outStream << comments1 << endl;        // reading line

outStream << comments2 << endl;

outStream << comments3 << endl;

outStream << comments4 << endl;

outStream << comments5 << endl;
```

```cpp
outStream << comments6 << endl;

outStream << comments7 << endl;

outStream << comments8 << endl;


for(int p = 0; p < Ivalue * Jvalue * Kvalue;p++)

{

outStream << scientific << setprecision(9) << (ivalue[p] - ivaluemin)/(ivaluemax -

ivaluemin)

 * precisioni << " " ;

if ((p+1)%5==0)

outStream << "\n" ;

}

outStream << "\n";

for(int p = 0; p < Ivalue * Jvalue * Kvalue;p++)

{

outStream << scientific << setprecision(9) << (jvalue[p] - jvaluemin)/(jvaluemax -

jvaluemin)

 * precisionj << " " ;

if ((p+1)%5==0)

outStream << "\n" ;

}

 outStream << "\n";

for(int p = 0; p < Ivalue * Jvalue * Kvalue;p++)
```

```
{

outStream << scientific << setprecision(9) << (kvalue[p] - kvaluemin)/(kvaluemax -

kvaluemin)

* precisionk << " " ;

if ((p+1)%5==0)

outStream << "\n" ;

}

outStream << "\n";

for(int p = 0; p < Ivalue * Jvalue * Kvalue;p++)

{

outStream << scientific << setprecision(9) << mvalue[p] << " " ;

if ((p+1)%5==0)

outStream << "\n" ;

}

outStream.close();

}
```

APPENDIX B

Matlab code to calculate CoV

% Calculate coefficient of variation from Fluent output file (node, x, y, z, vf2) for a cross-section

```
clc;

clear;

[filename1, pathname1] = uigetfile ('*.dat', ' Choose file');

[node, x, y, z, vf2] = textread (fullfile (pathname1, filename1), '%f %f %f %f %f ' );


sd = std (vf2)

avg = mean (vf2)

CoV = std (vf2) / mean (vf2)

DEVSQ = (length (vf2) -1) * (sd) ^2
```

APPENDIX C

Properties of the FGM (from Mori-Tanaka scheme)

Table I: Assuming Y-PSZ as the matrix phase and alumina as the particle phase

Y-PSZ Matrix (%)	Al_2O_3 Particle (%)	Young's Modulus (N/m²)	Poisson's Ratio	CTE (/°C)	Thermal conductivity (W/m/K)
100	0	2.00000E+11	0.3	1.03E-05	3
80	20	2.23300E+11	0.28767	9.78E-06	5.7018
60	40	2.49500E+11	0.27477	9.31E-06	8.6916
50	50	2.63684E+11	0.2682	9.08E-06	10.3106
40	60	2.78700E+11	0.2612	8.87E-06	12.022
20	80	3.11693E+11	0.24677	8.47E-06	15.7626
0	100	3.50000E+11	0.23	8.10E-06	20

Table II: Assuming alumina as the matrix phase and Y-PSZ as the particle phase

Y-PSZ Particle (%)	Al_2O_3 Matrix (%)	Young's Modulus (N/m²)	Poisson's Ratio	CTE (/°C)	Thermal conductivity (W/m/K)
100	0	2.00000E+11	0.3	1.03E-05	3
80	20	2.25000E+11	0.2865	9.75E-06	5.857
60	40	2.52120E+11	0.2729	9.27E-06	8.9491
50	50	2.66570E+11	0.2662	9.05E-06	10.5933
40	60	2.81640E+11	0.2593	8.84E-06	12.3091
20	80	3.13900E+11	0.2454	8.45E-06	15.9767
0	100	3.50000E+11	0.23	8.10E-06	20

Table III: Final averaged values

Y-PSZ (%)	Al_2O_3 (%)	Young's Modulus (N/m²)	Poisson's Ratio	CTE (/°C)	Thermal conductivity (W/m/K)
100	0	2.00000E+11	0.3	1.03E-05	3.00E+00
80	20	2.24150E+11	0.287085	9.77E-06	5.78E+00
60	40	2.50810E+11	0.273835	9.29E-06	8.82E+00
50	50	2.65127E+11	0.2672	9.07E-06	1.05E+01
40	60	2.80170E+11	0.26025	8.85E-06	1.22E+01
20	80	3.12796E+11	0.246085	8.46E-06	1.59E+01
0	100	3.50000E+11	0.23	8.10E-06	2.00E+01

REFERENCES

1). Benson, R. S., and J.W. Ponton, "Process Miniaturization- A Route to Total Environmental Acceptability?" Trans. IChemE, (V71, Part A, 1993), pp160-168.

2). Koeneman, P. B., I. J. Busch-Vishniac, and K. L. Wood, 1997, "Feasibility of Micro Power Supplies for MEMS," J. MicroElectoMechanical Sys. (V6, n4,), pp355-362

3). Paul, B. K., and R.B. Peterson, "Microlamination for Microtechnology-based Energy, Chemical, and Biological Systems," ASME IMECE, Nashville, Tennessee, November 15-20, 1999, pp45-52.

4). Martin, P. M., W. D. Bennett, and J. W. Johnson, "Microchannel Heat Exchangers for Advanced Climate Control," Proc. SPIE (v2639, 1996), pp82-88

5). Matson, D. W., P. M. Martin, W. D. Bennett, D. C. Stewart, and J. W. Johnson, "Laser Micromachined Microchannel Solvent Seperator," Proc. SPIE, (v3223, 1997), pp253-259.

6). Matson, D. W., P. M. Martin, A. Y. Tonkovich and G. L. Roberts, "Fabrication of a Stainless Steel Microchannel Microcombustor Using a Lamination Process," Proc. SPIE (v3514, 1998), pp386-392.

7). Tonkovich, A.Y.; Zilka, J.L.; LaMont, M.J.; Wang, Y. and Wegeng, R.S. "Microchannel reactors for Fuel Processing Applications," Chemical Engineering Science v 54 n 13 Sep 13-Sep 16 1998 1999 p 2947-2951 0009-2509

8). Paul, B.K. and T. Terhaar, "Comparison of two passive microvalve designs for microlamination architectures," J Micromech. Microengr. (v10, 2000), pp15-20.

9). Martin, P. M., D. W. Matson, W. D. Bennett, and D. J. Hammerstrom, "Fabrication of plastic microfluidic components," Proc. SPIE (v3515, 1998), pp172-176

10). Wegeng, R. S., C. J. Call, and M. K. Drost, "Chemical Systems Miniaturization," 1996 AIChE Spring Meeting, New Orleans, 1996.

11). Kakac, S. and H. Liu, 1997, Heat Exchangers-Selection, Rating, and Thermal Design, CRC Press, Boca Raton.

12). Kanlayasiri, K., and B.K. Paul, 2004, "A Nickel Aluminide Microchannel Array Heat Exchanger for High-Temperature Applications," accepted by *J. Mfg Proc.*.

13). Brooks, K. P., P. M. Martin, M. K. Drost, and C. J. Call, "Mesoscale Combustor / Evaoprator Development," ASME IMECE Conference, Nashville, TN, November 1999, pp37-43.

14). Wang, J. H., Yeh, H. Y. and Shyu, R. J., 1991, "Thermal-Hydraulic Characteristic of Microheat Exchangers," American Society of Mechanical Engineers, Dynamic Systems and Control Division (Publication) (DSC v32 Dec 1-6 1991), pp331-339.

15). Peng, X. F., B. X. Wang, G. P. Peterson, and H. B. Ma, " Experimental Investigation of Heat Transfer in Flat Plates with Rectangular Microchannels," International Journal of Heat and Mass Transfer (v38, n1, 1995), pp127-137.

16). Friedrich, C. R. and S. D. Kang, 1994, "Microheat Exchangers Fabricated by Diamond Machining," Precision Engineering, **16**, 1, pp56-59.

17). Paul, B. K., R. B. Peterson, and W. Wattanutchariya, "The Effect of Shape Variation on the Performance of High-Aspect-Ratio, Metal Microchannel Arrays," IMRET 3: Proceedings of the Third International Conference on Microreaction Technology, Springer-New York, 1999, pp53-61.

18). Jovanovic, G., J. Zaworski, T. Plant, and B. Paul, Proc. 3rd Intl. Conf. on Microreaction Technology, (Frankfurt, Germany), 1999.

19). Little, W. A., "Microminiature Refrigerators for Joule-Thomson Cooling of Electronic Chips and Devices," Advances in Cryogenic Engineering, (v33, 1990), pp. 1325-1333.

20). Paul, B.K., H. Hasan, J. Thomas, R. Wilson, and D. Alman, "Limits on Aspect Ratio in Two-fluid Micro-scale Heat Exchangers," *Transactions of NAMRC XXIX*, Gainesville, FL, 2001.

21). Gray, K.J., 2000, "Diamond and Related Materials", 9: (2), pp. 201-204

22). Jagannadham, K., 1999, J. Vac. Sci. Technol., A17: (2), pp. 373-379

23). Hui, P., Tan, H.S. and Lye, Y.S., 1997, IEEE Tran. Comp. Pack. & Manuf. Tech. Part A, 20: (4); pp. 452-457

24). Bower, M.B. and Mudawar, I., 1994, J.Electron Package, 116, pp. 290-297.

25). Gillot, C., Meysenc L., Schaeffer, C. and Bricard, A., 1999, IEEE Trans. Comp. Pack. Tech., 22: (3), pp. 384-389

26). Mizuno, Y., Kawasaki, A., and Watanabe, R., 1995, Metall. Mater. Trans., 26 B, p.75.
27). Zhang, L.M., Yuan, R.Z., Oomori, M. and Hirai, T., 1995, J. Mat. Sci. Let., 14, 22, p. 1620.

28). Liu et al., "Passive Mixing in a Three-Dimensional Serpentine Microchannel", Journal of Microelectromechanical Systems, Vol. 9, No. 2, June 2000, pp. 190-197.

29). Baker et al., "Laminar Flow in Static Mixers with Helical Elements", The Online CFM Book, http://baker.org/cfm, pp. 1-11

30). Shih, T.I.P. et al., "A Numerical Study of Flow and Heat Transfer in a Smooth and Ribbed U-Duct With and Without Rotation", ASME Journal of Hear Transfer, Vol. 123, April 2001, pp. 219-232

31).German, R.M., 1984, Powder Metallurgy Science, Metal Powder Industries Federation, Princeton, New Jersey.

32). Yeh, T. and Sacks, M.D., 1998, J. Am. Ceram. Soc., 71, 12, pp. C484-V487

33). Mori, T., and Tanaka, K., 1973, "Average Stress in Matrix and Average Elastic Energy of Materials with Misfitting Inclusions," Acta Metallurgica et Materialia, Vol. 21, pp. 571-574

34). Benveniste, Y., 1987, "A New Approach to the Application of Mori-Tanaka's Theory in Composite Materials," Mechanics of Materials, Vol.6, pp. 147-157.

35). Shin, H.W., Kwon, P. and Case, E.D., ASM Fall 2000 Proceedings.

36). Roeder, B.A., Sun, C.T., "Dynamic penetration of alumina/aluminum laminates: experiments and modeling", International Journal of Impact Engineering 25 (2001), pp. 169-185.

37). Stroock, A.D., Dertinger, S.K.W., Ajdari, A., Mezic, I., Stone, H.A., and Whitesides, G.M., "Chaotic mixer for microchannels." Science Magazine, 295, 2002.

38). Stroock, A.D., Dertinger S.K.W., Whitesides G.M., Ajdari, A. "Patterning flows using grooved surfaces." Analytical Chemistry, 74 (20): 5306-5312, 2002

39) Paul, Brian, Subramanian, Ramkumar and Kwon, Patrick "Understanding limits on fin aspect ratios in two-fluid micro-channel arrays produced by diffusion bonding", submitted to the ASME Journal of Manufacturing Science and Engineering, special issue on micro-mechanical manufacturing, 2004